The Astrophysical Journal, 920:30 (21pp), 2021 October 10 https://doi.org/10.3847/1538-4357/ac139d

The Picture of BLR in 2.5D FRADO: Dynamics and Geometry

Mohammad-Hassan Naddaf[1,2], Bożena Czerny[1], and Ryszard Szczerba[3]
[1] Center for Theoretical Physics, Polish Academy of Sciences, Lotnikow 32/46, 02-668 Warsaw, Poland; naddaf@cft.edu.pl
[2] Nicolaus Copernicus Astronomical Center, Polish Academy of Sciences, Bartycka 18, 00-716 Warsaw, Poland
[3] Nicolaus Copernicus Astronomical Center, Polish Academy of Sciences, Rabianska 8, 87-100 Torun, Poland
Received 2021 January 30; revised 2021 July 8; accepted 2021 July 11; published 2021 October 8

Abstract

The dynamics of the broad line region (BLR) in active galaxies is an open question; direct observational constraints suggest a predominantly Keplerian motion, with possible traces of inflow or outflow. In this paper we study in detail the physically motivated BLR model of Czerny & Hryniewicz based on the radiation pressure acting on dust at the surface layers of the accretion disk (AD). We consider here a nonhydrodynamical approach to the dynamics of the dusty cloud under the influence of radiation coming from the entire AD. We use here a realistic description of the dust opacity, and we introduce two simple geometrical models of the local shielding of the dusty cloud. We show that the radiation pressure acting on dusty clouds is strong enough to lead to dynamical outflow from the AD surface, so the BLR has a dynamical character of a (mostly failed) outflow. The dynamics strongly depends on the Eddington ratio of the source. Large Eddington ratio sources show a complex velocity field and large vertical velocities with respect to the AD surface, while for lower Eddington ratio sources vertical velocities are small and most of the emission originates close to the AD surface. Cloud dynamics thus determines the 3D geometry of the BLR.

Unified Astronomy Thesaurus concepts: Galaxy accretion disks (562); Radiative processes (2055); Broad-absorption line quasar (183); Quasars (1319); Astrophysical dust processes (99); Gas-to-dust ratio (638); Active galactic nuclei (16); Active galaxies (17); Reverberation mapping (2019); Supermassive black holes (1663); Galaxy winds (626); Dust continuum emission (412)

1. Introduction

Broad emission lines are the most characteristic features of the optical/UV spectra of most active galaxies. They were the motivation of the study by Seyfert (1943), and they provided the clue to the puzzle of the quasar phenomenon (Schmidt 1963). The intense emission of broad line regions (BLRs) from the X-ray to optical to infrared has been studied for years (Boroson & Green 1992; Lawrence et al. 1997; Reeves & Turner 2000; Sulentic et al. 2000; Gaskell 2009; Le & Woo 2019; Raimundo et al. 2020). These studies rely on the analysis of the spectra and their time dependence because the region is messy, turbulent, and not yet easily spatially resolvable. Line shapes and the photoionization conditions of their formation imply that BLR emission consists of two line categories: high-ionization lines (HIL) and low ionization lines (LIL; Collin-Souffrin et al. 1988). Further research brought a wealth of information on the spatial distribution of the medium, its motion, and the thermal and ionization state of the material (for a detailed review, see Netzer 2013), but did not bring a definite answer to the question of the origin of the material located in the BLR.

The reverberation mapping (RM) approach based on the delayed response of BLR material to variations of the active galactic nucleus (AGN) continuum (Blandford & McKee 1982; Peterson 1993) enabled us to precisely measure the spectral-dependent radius of BLRs (Wandel et al. 1999). It also brought us an insight into the motion of the BLR (Peterson et al. 1998), showing that its dynamics is a composition of a Keplerian motion around the black hole (BH), and a turbulent motion that gives overall a complex velocity field (Shapovalova et al. 2010; Grier et al. 2013).

That said, the presence of observational signatures of inflow/outflow (e.g., Brotherton et al. 1994; Done & Krolik 1996) makes the origin of this material puzzling. Reasonable possible origins of the material are the accretion disk (AD) and the interstellar medium. The recently confirmed flattened geometry of the BLR, resolved observationally for the first time in two sources (Gravity Collaboration et al. 2018, 2021), may favor the first possibility, i.e., the material originates from the AD; and also recent observation-based studies (Leftley et al. 2019; Mas-Ribas 2019; Mas-Ribas & Mauland 2019) show that radiation pressure, likely on the multiphase medium, is the prevalent mechanism responsible for the outflows in quasars.

There have been many attempts by different researchers to explain the formation and dynamics of BLR clouds in a theoretical context over last 50 years. The first attempt was to simply model the emission line formation by studying the photoionization equilibrium (Osterbrock 1978), which did not explain the BLR formation mechanism and dynamics (Capriotti et al. 1980). The idea of magnetically driven winds was then initiated by Blandford & Payne (1982), in which the magnetocentrifugal force was responsible for driving the outflow to explain the BLR formation. Although the mechanism requiring a strong large-scale poloidal component of the magnetic field was not self-consistent (Balbus & Hawley 1991), dusty molecular torus and X-ray absorption features could be explained (Elitzur & Shlosman 2006; Fukumura et al. 2015; Huang et al. 2020). It was then proposed by Begelman et al. (1983) that the outer disk that is irradiated by central source to the Inverse Compton temperature can give rise to the formation of thermally driven winds that could be the origin of BLR. This also required additional elements to be assumed, such as a hot corona above the disk or an inner hot flow (Witt et al. 1997; Blandford & Begelman 1999). Radiatively line-driven winds as a mechanism for BLR formation, first studied by Murray et al. (1995), was the next theoretically based attempt that was particularly/exceptionally successful at predicting the line

profile shapes. This model most likely explains the HIL part of BLR emission, where line profiles show signatures of outflow. However, even a line-driven wind does not always escape, and a failed wind may form at some range of radii (Risaliti & Elvis 2010), thus complicating the line profile predictions. Inflow models (Done & Krolik 1996, followed by others, e.g., Hu et al. 2008 and Wang et al. 2017), in which the flow of material from large radii was considered to be responsible for BLR formation, also came under attention, but they lack predictive power. BLR formation due to disk instabilities, also known as formation in situ, has also been given attention for years (Collin & Zahn 1999, 2008; Wang et al. 2011, 2012b).

Radiatively dust-driven models are the newest models for BLR formation focusing on the radiation pressure of the AD, and also the presence of dust at large radii. The latter is hinted at in a number of papers (Rees et al. 1969; Rieke 1978; Barvainis 1987; Dong et al. 2008). This dust is usually considered to constitute the dusty/molecular torus, but dust can exist also closer in, if shielded, and may play a role in BLR formation. The models in this category are the Failed Radiatively Accelerated Dusty Outflow (FRADO) model (Czerny & Hryniewicz 2011), and a model by Baskin & Laor (2018) in which the static disk is inflated due to irradiation in the dusty part (hereafter BL18). In this work, we intend to study the dynamics of the BLR based on the FRADO model. Here, we concentrate on the semi-analytical description of the cloud motion that will later allow one to calculate the BLR transfer function and line shapes, and to compare these predictions to parametric models assuming an arbitrary cloud distribution. In this way we aim to test whether FRADO is a viable model of the LIL part of the BLR.

Due to various motivations such as estimating the central BH mass, simulating the dynamics of BLR material due to radiation pressure, either in lines or on dust, has been of high interest for researchers (e.g., Marconi et al. 2008; Netzer & Marziani 2010; Wang et al. 2012a; Plewa et al. 2013; Shadmehri 2015; Khajenabi 2016). Different geometries, and even the time-dependent case of the radiation field have been investigated in the existing literature (e.g., Saslaw 1978; Mioc & Radu 1992; Krause et al. 2011; Liu & Zhang 2011). Some studies based on radiation pressure including hydrodynamical (HD) ones do not use a realistic prescription for the radiation field of the AD. Either the disk has been initially considered as a point-like source with a luminosity (e.g., Donea & Protheroe 2002; Mosallanezhad et al. 2019), or it is treated as an extended object with only the radial component of the force (in spherical coordinates) used in the computations (e.g., Risaliti & Elvis 2010). Both cases result in the radiation field being proportional to the inverse square of the distance, so the radiation field ultimately has the form of a repelling central force and never produces a strong vertical component close to the disk surface to lift the material sufficiently before being repelled outward. This can be applicable if the BLR extends far beyond the outer radius of the AD, e.g., in BLR models based on cloud inflow from larger radii (Wang et al. 2017), but this scenario is not firmly established. Instead, there are arguments that the BLR instead overlaps with the AD (e.g., Czerny et al. 2004b). There are also a number of studies (e.g., Proga et al. 1998, 2000; Proga & Kallman 2004; Nomura et al. 2020; Mizumoto et al. 2021) that address the full disk radiation field but focus on the line-driving force in which the element of dust is missing.

Intuitively, the radiation force acting on clouds in the vicinity of the AD is not radial but almost plane-parallel. This case has been investigated in the FRADO model analytically, but only in one dimension and for a very local flux (Czerny et al. 2015, 2017). This 1D model roughly reproduces the overall BLR position without including the arbitrary parameters, but the line shapes based on this local model always showed traces of the double-peaked structure, the vertical acceleration was not as efficient as required, and they did not show the characteristic Lorentzian wings observed in high Eddington ratio sources. The line shapes improved when a much higher wavelength-averaged dust opacity was used instead of the standard $\kappa = 8\,(\mathrm{cm}^2\,\mathrm{g}^{-1})$, but it was not clear that such opacity requirements were realistic. Thus, the issue of the radiation field of an extended disk must be addressed for which the net radiation force is a complex function of cloud position. Reaching a realistic prescription for the radiation of an AGN and the resulting outflow will be of high importance, not only particularly in the physics of the BLR, but also generally in AGN feedback and in star formation in host galaxies (Croton et al. 2006; Raouf et al. 2019).

The radiation field of an extended luminous disk was first calculated by Icke (1980) in a wavelength-averaged form. The method was only then followed in some papers (Pereyra et al. 1997; Proga et al. 1998, 1999; Feldmeier & Shlosman 1999; Watarai & Fukue 1999; Proga et al. 2000; Hirai & Fukue 2001; Proga & Kallman 2004; Nomura et al. 2020). We present a detailed note on the calculation of radiation field of an extended disk in the Appendix of this paper and in a very generic form capable of being folded with wavelength-dependent dust opacities.

Although the proposed theoretical attempts mentioned above could somehow explain the formation of the BLR along with some features of an AGN's spectrum, they have not been able to self-consistently explain the dynamical behavior of the BLR and its geometry altogether, which we have from observational data, especially RM-based data. Hence, approaching a unified self-consistent theoretically based model that can explain the formation, geometry, and dynamics of the BLR is highly required. The 3D FRADO model is expected to recover observationally known features of a BLR, i.e., the radius or equivalently the time-delay, the complex velocity field, and line profiles, all self-consistently without the need of any arbitrary parameter(s). In this work we especially focus on the dynamics and geometry of the BLR as the first step.

We therefore introduce our 3D FRADO model in detail in Section 2. The model does not go through HD calculations, so the effects of the pressure gradients are neglected. However, based on our results provided in Section 3, most of the time clouds (assumed to be pressure confined) move at supersonic velocities (likely along with the surrounding medium due to dynamical coupling), so we preferably limit ourselves to the relatively simple and computationally efficient non-HD version of our model. We will then test in the next paper how much the model successfully catches the overall dynamical properties and explains the observational properties of the BLR, such as line shapes, average time delays and transfer functions for LIL lines such as Hβ and Mg II. The results are then followed by a discussion in the last Section 4, where the advantages of our approach over other available BLR models including parametric models and hydro models are also addressed.

2. 3D FRADO Model With Wavelength-dependent Opacity

The basic FRADO model (Czerny & Hryniewicz 2011; Czerny et al. 2015, 2016, 2017) described the failed dusty wind motion in a 1D approximation; i.e., the motion vertical to the disk plane was included, apart from the rotational velocity. In addition, the wavelength-averaged dust opacity was used. The radiation from the central region was only included in computations of the dust evaporation and neglected in the dynamics, which was determined only by the local flux of the AD. This approximation was necessary to formulate a semi-analytical model of the dynamics. However, the radiation pressure from the entire disk in this model is not properly represented, and the proper description of the dust interaction with the radiation field is also critical for the model.

In this paper we formulate the full 3D model describing the motion of the initially dusty clouds under the radiation pressure coming from the entire AD and the gravity of a central supermassive black hole. We assume that the mass of the AD is much smaller than the BH mass and its gravitational field is negligible. The net radiation force is neither radial nor vertical, but instead a complex combination of both, and the clouds before being accelerated have a circular motion along a local Keplerian orbit at the disk surface layers, so the resulting motion of a cloud forms a complex 3D trajectory. The net acceleration is

$$\boldsymbol{a}^{\rm net} = \boldsymbol{a}^{\rm gra} + \boldsymbol{a}^{\rm rad}(< T_{\rm s}) \tag{1}$$

where $\boldsymbol{a}^{\rm gra}$ stands for the gravitational field of the central BH, and $\boldsymbol{a}^{\rm rad}$ is the acceleration due to radiation pressure of the AD given in its general form (find the detailed version in the Appendix: Equation (A15)) by

$$\int_{\lambda_i}^{\lambda_f}\int_{\boldsymbol{S}} f(I_\lambda, K_\lambda^{\rm abs}, K_\lambda^{\rm sca}, \Psi, \boldsymbol{r}, \cdots) d\boldsymbol{S}\, d\lambda \tag{2}$$

where I_λ is the radiation intensity of the AD specified in Section 2.1; Ψ, $K_\lambda^{\rm abs}$, and $K_\lambda^{\rm sca}$ are the dust-to-gas ratio, total absorption opacity, and total scattering opacity of the clump, respectively (see (A22)–(A25)), and λ_i and λ_f define the range of effective wavelengths for an adopted dust model, all addressed in Section 2.2; $\boldsymbol{r}$ is the position vector of the clump; ($<T_{\rm s}$) implies that the radiative acceleration is available as long as the dust temperature calculated in the cloud along the trajectory is less than that of the dust sublimation temperature $T_{\rm s}$, otherwise dust evaporates and the cloud performs later just a ballistic motion in the gravitational field of the BH (Section 2.3); and $\boldsymbol{S}$ is the surface of the AD or part of it, as discussed in Section 2.4 on the shielding effect.

2.1. Properties of Underlying AD–BH System

We assume the source of the radiation field is represented by an extended optically thick, geometrically thin disk, described by the Shakura & Sunyaev (1973) standard model (SS73). The inner disk radius is set at $R_{\rm in} = 6R_g$, and the outer radius is located at $R_{\rm out} = 10^6 R_g$ in all models, where R_g is the gravitational radius of the BH defined as $R_g = GM_{\rm BH}/c^2$. The flux density is locally described as in SS73, including the no-torque inner boundary conditions

$$\mathbb{F}(R) = \frac{3G\dot{M}_{\rm edd}}{8\pi}\frac{M_{\rm BH}\,\dot{m}}{R^3}\left(1 - \sqrt{\frac{R_{\rm in}}{R}}\right), \tag{3}$$

and the locally emitted flux is represented as blackbody emission; i.e., the intensity is given by the Planck function

$$I_\lambda = B_\lambda(T(R, \varphi)). \tag{4}$$

The AD flux is thus described by the central BH mass, set as $M_{\rm BH} = 10^8 M_\odot$, corresponding to the mean value in the quasars catalog of Shen et al. (2011), for which

$$R_g = 4.7867 \times 10^{-6}\,({\rm pc}) = 0.0057\,({\rm lt\text{-}day}) \tag{5}$$

and the dimensionless accretion rate, $\dot{m}$, is normalized to the Eddington value for the adopted $M_{\rm BH}$

$$\dot{M}_{\rm edd} = 1.399 \times 10^{26}\,({\rm g\ s^{-1}}). \tag{6}$$

In this paper, we stick to three values of the dimensionless accretion rate: $\dot{m} = 0.01$ and 0.1 (low Eddington ratios), and $\dot{m} = 1$ (high Eddington ratio).

The description of SS73 for the flux of a nonrelativistic radiatively efficient AD provides us with an azimuthally symmetric profile for the effective temperature of the AD as a function of radius R, since

$$\mathbb{F} = \sigma_{\rm SB}\, T_{\rm eff}^4(R), \tag{7}$$

where $\sigma_{\rm SB}$ is the Stefan–Boltzmann constant; so

$$T(R, \varphi) = T_{\rm eff}(R). \tag{8}$$

2.2. Dust Opacity

In general, the radiation pressure acting on a BLR cloud should be a combination of absorption in lines and absorption/scattering on dust. In the FRADO model, aimed at modeling the LIL part of the BLR, we assume that the dust processes dominate. In this case, in contrast to the line-driven winds in which the Doppler effect is important, the absorption efficiency does not depend on the cloud velocity, and the equations given in the Appendix include this assumption. However, the effect depends on the assumption of the dust chemical composition, grain sizes, and the dust-to-gas mass ratio.

The value of K_λ can be obtained using prescriptions from Röllig et al. (2013) and Szczerba et al. (1997) for different dust models with a given distribution of dust types and grain sizes. See Equation (A24) for details on how to find K_λ assuming a given dust model with a certain distribution. We further assume the classical MRN dust model appropriate for the interstellar medium (Mathis et al. 1977), as also used in the BL18 model. This simple model consists of silicate and graphite grains. Signatures of silicate in AGNs are seen (Netzer et al. 2007), and the equilibrium temperature of the grains implies the presence of graphite (Clavel et al. 1989). However, amorphous carbon grains rather than graphite are most likely expected based on UV spectra (Czerny et al. 2004a), and/or the grain size range is not typical (Gaskell et al. 2004), as the overall extinction curve is more similar to an SMC curve than to the typical graphite-dominated Milky Way curve (e.g., Richards et al. 2003; Hopkins et al. 2004; Zafar et al. 2015). The actual content of the AGN dust is still under vigorous study (Chau Giang & Hoang 2020), but we adopt here the classical approach. The grain size distribution in the MRN model is

identical and given by

$$dn_i(a) = n\ A_i\ a^{-3.5}\ da, \qquad 0.005 \leqslant a \leqslant 0.25\ (\mu\mathrm{m}) \quad (9)$$

where a is the grain size (radius), i stands for the dust type, and A_i is the normalization constant that determines the overall abundances of the grain type, which directly leads to a unique value for the dust-to-gas mass ratio Ψ (see Equation (A25)). For example, setting $A_{\mathrm{silicate}} = 10^{-25.10}$ and $A_{\mathrm{graphite}} = 10^{-25.13}$ (Weingartner & Draine 2001) in the MRN dust model, one can obtain $\Psi = 0.00955$ (Röllig et al. 2013). We set $\Psi = 0.005$, thus adopting the mean value of the Milky Way (Mathis et al. 1977). The dust-to-gas ratio in quasars has not been yet sufficiently studied, so a firm value or range of values in this context is not yet available. However, a value of almost 0.008 is estimated for an AGN sample (Shangguan et al. 2018), and also a recent study by Jun et al. (2021) has addressed the dust-to-gas ratio in obscured quasars. K_λ is independent of dust type and abundances. The MRN dust model is taken for simplicity and realistic modeling of AGN dust content must be addressed in future studies.

Here, we assume that the coupling between the dust and the gas is strong. The friction thus prevents dust from moving faster than the gas and momentum is transferred to the gas, so the dusty/gaseous cloud moves as a single entity. The coupling is generally quite effective in dense media, for example, in star-forming molecular clouds (e.g., Hosseinirad et al. 2018; Reissl et al. 2018). The local gas number density (n_{H}) of the BLR clouds is rather high, with most recent estimates for the LIL BLR of order 10^{12} cm^{-3} (e.g., Adhikari et al. 2016; Panda et al. 2018, 2019a, 2019b, 2020a, 2020b; Panda 2020), so this assumption should be satisfied.

2.2.1. The Possibility of Outflow Launching in FRADO

We first test if the AD surface can be a source of the wind outflow under the effect of radiation pressure. Czerny et al. (2015, 2017) argued that in the upper part of the AD atmosphere the Planck mean opacity is much larger than the Rosseland mean opacity used in the disk interior, so the disk is not considerably puffed up, and this larger Planck value, appropriate for wind driving, will lead to an outflow. However, BL18 postulated that the AD atmosphere, with dust included, will remain static. So, first we check whether indeed the condition postulated by the FRADO model is satisfied if the realistic description of the opacity is included.

For this purpose, we calculated the value of the Planck mean opacity as a function of the AD radius (or, equivalently, as a function of the AD effective temperature) for the typical values of the model global parameters: $\dot{m} = 0.1$ and $M_{\mathrm{BH}} = 10^8 M_\odot$, as shown in the Figure 1. We integrated the wavelength-dependent dust opacity in the whole wavelength range, from $\lambda_i = 6.1995$ (nm) to $\lambda_f = 1.2399$ (mm). The aim was to compare it with the Rosseland mean, which was used to determine the AD vertical structure needed to get the AD height.

The Rosseland mean was calculated for the same range of radii, at the position of the bottom of the AD photosphere, $\tau = 2/3$. This Rosseland mean, depending on density and temperature, comes from the tables that include dust, molecules, atomic opacities, and Thomson scattering (for details, see Różańska et al. 1999).

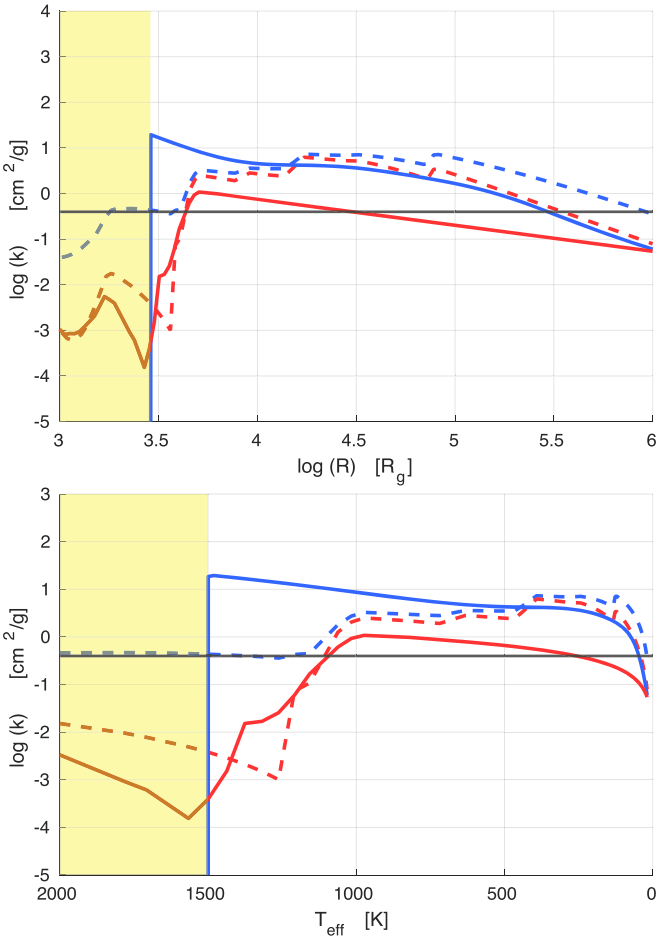

Figure 1. The upper panel shows the radial dependence of the Planck mean (blue solid line) and the Rosseland mean (red solid line) for $\dot{m} = 0.1$ and $M_{\mathrm{BH}} = 10^8 M_\odot$ as used in the paper. The viscosity for the calculation of the Rosseland mean is set to be 0.02. The Planck (blue dashed line) and Rosseland (red dashed line) mean from the code of Semenov et al. (2003) for the density profile from the disk atmosphere are compared to our values. The lower panel displays the values in terms of the equivalent effective temperature of the AD. The black solid lines in both panels show the ratio of the Thompson cross section to the mass of a proton. The regions shaded in yellow show where the temperature is above that of dust sublimation.

In our calculation of the Planck mean, we multiply the result by Ψ because, due to gas−dust coupling, the gas content of the clump hitchhikes with the dust. However, as the gas contribution to the opacity is not included, the Planck mean formally shows a sudden drop to zero at the dust sublimation temperature. We see that the Planck mean is always higher than the Rosseland mean, which provides an argument in favor of the scenario in which the dusty wind launches from the AD surface.

Since our opacities are not the most accurate, we check this result using the code[4] described in Semenov et al. (2003) and calculating the Planck and Rosseland mean for the dust and gas material. We used the gas number density profile (n_{H}) from the AD atmosphere, which varied from 1.37×10^{14} cm^{-3} to 3.88×10^9 cm^{-3} at the outer radius. These computations also imply that the Planck mean is higher than the Rosseland mean, and the idea of the dynamical character of the BLR is well supported.

[4] https://www2.mpia-hd.mpg.de/~semenov/Opacities/opacities.html

We have to stress, however, that the use of Planck mean values of the opacity does not fully represent the driving force due to radiation pressure, as given by Equation (A15). In the actual computations we use the wavelength-dependent opacity, and the force acting on the particle is calculated by folding this opacity with the radius-dependent and spectral-dependent radiation flux.

2.3. Dust Temperature

If the dust in the cloud is overheated, it evaporates rapidly. Therefore, at each cloud position we calculate the dust mean temperature by integrating the heat absorbed by the grains embedded in the cloud and comparing it to the total cooling of all of the grains, independent of their size.

Dust cools down by instantaneous re-emission of the absorbed radiation in the form of isotropic blackbody radiation, as long as the dust temperature is below that of sublimation, so

$$Q_{\rm abs} = Q_{\rm emit}(<T_{\rm s}). \tag{10}$$

Once $Q_{\rm abs} = Q_{\rm emit}(T_{\rm s})$ the dust content of the clump evaporates and the clump follows a subsequent ballistic motion falling back to the disk surface. See the Appendix (A.3) for details. This is a certain simplification, since the carefully calculated dust temperature depends on the grain type and grain size. However, as we have to perform the temperature computations for each point of each cloud trajectory, this much less time-consuming approximation is justified.

We later assume the fixed specific value of the dust evaporation temperature of 1500 K (e.g., Barvainis 1987; Li 2007; Figaredo et al. 2020; Huang et al. 2020), for all species and sizes, and we assume that the process happens instantaneously. The evaporation is indeed fast, of order 1 day (see BL18). Although the temperature of 1500 K is a sort of mean value for all grain sizes and species, the assumption of a single temperature is much less justified (BL18, Tazaki et al. 2020; Temple et al. 2020) and has to be treated as a first approximation. However, in our dynamical model, computations of the selective evaporation would be too time consuming, though it could have been done in the BL18 model.

2.4. Shielding Effect

According to radiatively driven wind models, launching an efficient outflow is not possible if the launching region is not shielded from irradiation by the central source (see, e.g., Gallagher & Everett 2007; Proga 2007; Higginbottom et al. 2014). This protection from intense central radiation, the so-called shielding effect, was first generally postulated by Shlosman et al. (1985) and later by Voit (1992) to justify the presence of polycyclic aromatic hydrocarbons (PAHs) in AGNs. It was first modeled by Murray et al. (1995), who assumed a bulk of dense gas at the inner edge of the line-wind launching region to block soft X-rays.

The shielding can be naturally caused by other phenomena: other clouds (Kartje et al. 1999); the wind itself because of the high-ionization parameter and high column density at the inner edge of the wind known as a "warm absorber" (Murray & Chiang 1995); a magnetocentrifugal wind (Everett 2005); the innermost failed winds first found in hydrodynamical simulations by Proga et al. (2000); or the disk itself (Wang et al. 2014). Thus the apparently necessary shielding, particularly close to the disk surface, protects the wind medium from becoming over-ionized and likely prevents the radiation from the central parts to reach the distant disk regions (Miniutti et al. 2013).

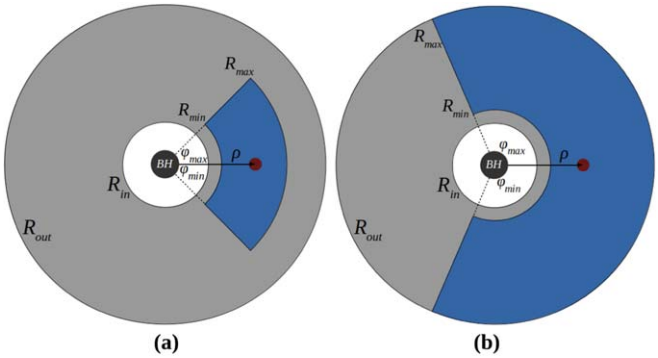

Figure 2. Geometry of (a) the α-patch and (b) the β-patch shielding models. The cloud is exposed to a part of the disk radiation marked in blue. The size and location of these blue regions change as the cloud moves. The integral of the radiation pressure to calculate the radiative force is integrated over the area of the disk shaded in blue, depending on the shielding model adopted.

There are many studies that hint at the importance of the shielding effect and model it (see, e.g., Proga & Kallman 2004; Risaliti & Elvis 2010; Sim et al. 2010; Higginbottom et al. 2013; Nomura et al. 2013; Hagino et al. 2015; Mizumoto et al. 2019).

In order to incorporate the shielding effect into our model, or indeed to mimic the physical action of the complex multiphase surroundings, we introduce two simple geometries. In our preliminary study of the shielding effect (Naddaf et al. 2020), we found that these two models conveniently catch the required properties. However, in this paper we reintroduce them with some changes to their names and geometrical properties to make them mathematically and intuitively more intelligible.

2.4.1. The α-patch Model

As the simplest form of shielding, we consider the contribution from a small polar patch to the radiation pressure acting on the clump. We assume here that the cloud is exposed only to the radiation from the small part of the disk, centered below the cloud position, and the size of the patch is always proportional to the actual height of the cloud. Thus the position and the size of the patch varies as the cloud moves. A cloud very high above the disk is exposed to a large fraction of the disk. This approach mimics the fact that a given cloud is actually embedded in the rising clumpy wind, and this clumpy wind is much denser close to the disk surface, so the radiation cannot easily penetrate the medium in the direction roughly horizontal to the disk plane. This geometry is illustrated in Figure 2(a). As a model parameter, α, we introduce the ratio of the cloud height to the patch size, which is fixed during the cloud motion.

In order to incorporate this model into our computations, we apply the below upper and lower limits in the calculation of the integral of the radiative force:

$$\begin{aligned} R_{\rm min} &= \rho - \alpha z \\ R_{\rm max} &= \rho + \alpha z \\ \varphi_{\rm min} &= -\pi\left(\frac{\alpha z}{\rho - R_{\rm in}}\right) \\ \varphi_{\rm max} &= \pi\left(\frac{\alpha z}{\rho - R_{\rm in}}\right). \end{aligned} \tag{11}$$

2.4.2. The β-patch Model

In this shielding model, the contribution of radiation pressure from a wider field of view is considered, compared to that in the α-patch model. Although we still have a polar patch acting on the clump, we examine how the consideration of a wider azimuthal angle and also of the outer part of the AD affects the motion of clumps and the overall shape of the BLR. We intend with this model to mimic the possible asymmetry of the shielding; i.e., the fact that the outer part of the disk and the azimuthally extended region excluding the central disk may be visible to the cloud. In this model, the outer radius of the patch is always $R_{\rm out}$ of the AD, the inner radius is proportional to the actual height of the cloud, and the patch is azimuthally extended by $\pi/2$. This geometry is shown in Figure 2(b). The geometrical properties of the patch varies as the cloud moves. So, in this model, again the increasing cloud height implies an increasing exposure to the disk radiation.

Therefore, the upper and lower limits for the integral of radiative force are:

$$\begin{aligned} R_{\rm min} &= \rho - \beta z \\ R_{\rm max} &= R_{\rm out} \\ \varphi_{\rm min} &= -\frac{\pi}{2}\left(1 + \frac{\beta z}{\rho - R_{\rm in}}\right) \\ \varphi_{\rm max} &= \frac{\pi}{2}\left(1 + \frac{\beta z}{\rho - R_{\rm in}}\right). \end{aligned} \tag{12}$$

The computation of the radiative force acting on the cloud presented in the Appendix (Equation (A15)) is general. If the shielding effect is assumed, the integration is performed only for a fraction of the disk surface as set in Equations (11) and (12). In order to neglect the shielding, one needs to set

$$\begin{aligned} R_{\rm min} &= R_{\rm in} = 6\ R_g \\ R_{\rm max} &= R_{\rm out} = 10^6\ R_g \\ \varphi_{\rm min} &= 0 \\ \varphi_{\rm max} &= 2\pi. \end{aligned} \tag{13}$$

2.5. Cloud Dynamics

In the present model we neglect the effects of general relativity and use just Newtonian dynamics because, at the distance of the BLR, these effects are usually relatively unimportant.

The clouds are not allowed to cross the disk surface, so we also calculate the AD shape as a function of radius. We do that using the code from Różańska et al. (1999), neglecting the effects of self-gravity on the disk structure (see, e.g., Czerny et al. 2016, and the references therein). The disk thickness depends on the viscosity parameter, which we set as visc. = 0.02 in our computations, motivated by the variability studies of AGNs (Grzedzielski et al. 2017, and the references therein).

Clouds can be practically launched either from the disk surface or above it; the second approach illustrates the possible effects of cloud collisions. We only focus on launching from the disk surface (with zero vertical velocity). Clouds can be launched at an arbitrarily large radius, but basically we set the launching radius to be lower than the outer disk radius so that the clouds see the radiation field of the whole extended disk, and the radiation force—its direction and value—has to be calculated by integration over the disk surface. We consider models in which the clouds see all of the disk emission, but also we formulate models with the shielding effect included. The inner radius for launching the clouds from the disk surface is actually the site of the onset of the BLR, shown in Figure 3 as $\rm BLR_{in}$, or in other words, the inner radius of the BLR for specified values of $M_{\rm BH}$ and $\dot{m}$ is set by the condition that a cloud can be launched.

3. Results

We formulated the 3D version of the FRADO model of the BLR. Our model does not (almost) have arbitrary parameters, apart from the values of the BH mass, $M_{\rm BH}$, and the accretion rate, $\dot{m}$ in Eddington units. The basic remaining free parameter is the dust sublimation temperature, $T_{\rm s}$. These three values of $M_{\rm BH}$, $\dot{m}$, and $T_{\rm s}$ determine the geometrical properties of the BLR and the 3D motion of the clouds. The disk height value needed for the vertical position of cloud launching depends on the viscosity parameter in the SS73 model, and if shielding is considered, one more parameter characterizes its geometry. In the present paper, we have concentrated on the tests of the dynamical aspects of the model and the resulting geometry of the BLR.

For this purpose, we have set the model parameters as below:

$$\begin{aligned} M_{\rm BH} &= 10^8\ M_\odot \\ \dot{m} &= 1 \text{ (High Eddington rate)} \\ \dot{m} &= 0.1,\ 0.01 \text{ (Low Eddington rates)} \\ T_{\rm s} &= 1500 \text{ (K)} \\ \text{visc.} &= 0.02 \\ \alpha &= 3,\ 5 \\ \beta &= 3,\ 5 \\ \Psi &= 0.005 \text{ (MRN)}. \end{aligned} \tag{14}$$

3.1. Sublimation Location

Calculating the geometrical location at which the relation $Q_{\rm abs} = Q_{\rm emit}(T_{\rm s})$ holds, called the *sublimation location* and denoted by $S(R)$, we divide the space above the disk into two regions of *dust sublimation* and *dust surviving*, as shown in Figure 3. The crossing radius of the $S(R)$ and disk surface yields the radius at which dust gets sublimated at the disk surface, known as $\rm BLR_{in}$. It sets the inner radius for the launching of the clouds, as shown in Figure 3. Theoretically, BLR material can be present up to a radius known as $\rm BLR_{out}$, which is shown in Figure 3 and defined by the condition that dust can survive irradiation by the entire disk if the radiation field is spherical.

Without inclusion of the shielding effect, the function $S(R)$ has a bowl-like form (when viewed in 3D; e.g., Kawaguchi & Mori 2010, 2011; Czerny & Hryniewicz 2011; Goad et al. 2012; Oknyansky et al. 2015; Figaredo et al. 2020), while including shielding results in a more funnel-like shape.

These two values of $\rm BLR_{in}$ and $\rm BLR_{out}$ set the radial domain of our computations of the motion and trajectories of clouds. We have previously computed them and the function of $S(R)$, as available in Naddaf et al. (2020) for different values of α (or β) and also for the case with no shielding. Note that due to our change in the mathematical illustration of shielding models, the previous β behaves like $1/\beta$.

3.2. Examples of 3D Motion of a Cloud

When the clouds are initially located at the disk surface, dusty wind is not launched without a shielding effect, as the disk surface, without any protection, becomes overheated.

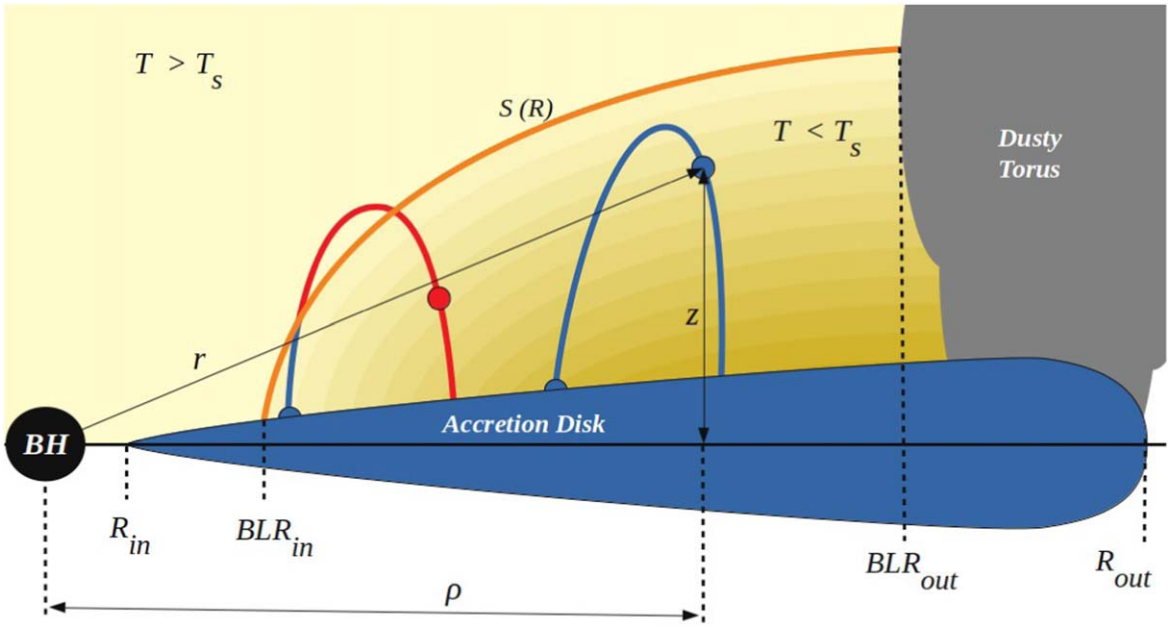

Figure 3. Schematic illustration of the 3D FRADO mechanism. The inner and outer radius of the AD are denoted by R_{in} and R_{out}, respectively. The curved line in orange represents the *sublimation location*, $S(R)$; above this, marked by ($T > T_s$), is the region where dust disappears due to intense radiation from the central parts of the AD and is called the *dust sublimation* region. The region restricted between the disk surface and $S(R)$ marked by ($T < T_s$) is called the *dust surviving* region, where the temperature of the dust is below that of sublimation. The onset of the BLR, BLR_{in}, is an innermost radius from which a cloud can be launched. BLR_{out} sets the inner radius of the *conceptual* torus and the outer radius of the BLR. A dusty clump being launched from the AD surface remains dusty (trajectory in blue) unless it reaches to $S(R)$, where it then loses the dust content and follows a ballistic motion (trajectory in red). Due to azimuthal symmetry, the position of the clump is described in the cylindrical coordinates. The radial position of the clump is denoted by ρ to make it distinguishable from the integrand component of R of the AD in the calculation of the radiation pressure (see the Appendix: Figure 10(b), and Equation (A15)). However, ρ and R are the same in nature, so for simplicity, we use R or *Radius* in all plots. The vertical position of the clump denoted by z is measured from the equatorial plane, to which we refer by z or *Height* in all plots.

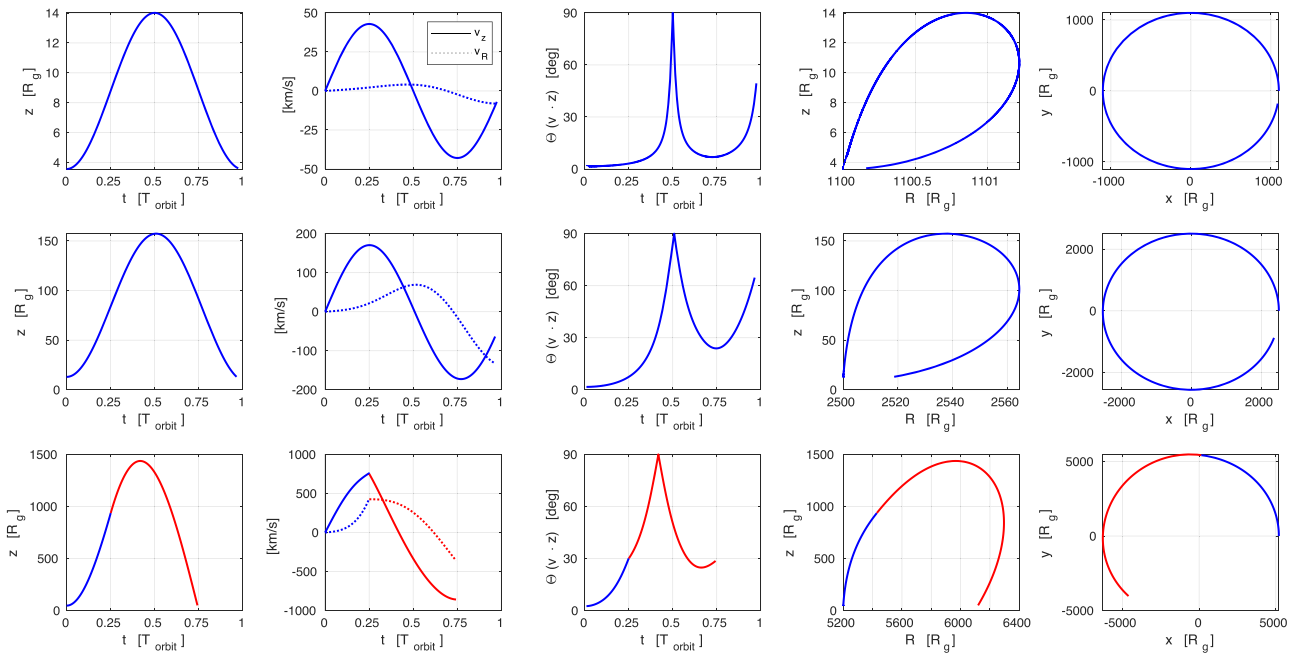

Figure 4. Examples of motion for the α-patch model with $\alpha = 3$. The results are shown for $\dot{m}$=0.01 (upper panels), 0.1 (middle panels), and 1 (lower panels). The disk surface is not depicted. The motion of the dusty cloud is shown in blue. Once the dust content of the cloud is sublimated, the subsequent ballistic motion is shown in red. Variables x and y are coordinates in the equatorial plane of the AD, so that $R^2 = x^2 + y^2$. The actual radial and vertical position and velocity of the model cloud in cylindrical coordinates are denoted by R, z, v_R, and v_z, respectively. The temporal axis is denoted by t in units of local Keplerian orbital time ($T_{\rm Orbit}$). The middle column of panels shows the angle between the velocity vector of the cloud and the normal vector of equatorial plane in the frame locally co-moving with the disk. For these exemplary motions, an arbitrary launching radius of $R = 1100R_g$, $2500R_g$, and $5200R_g$ are chosen for $\dot{m} = 0.01$, 0.1, and 1, respectively.

However, if shielding is postulated, the initial outflow is easily launched. In Figure 4 we show several examples of individual cloud trajectories. The path covered by a dusty cloud is marked in blue, and in cases where the cloud was exposed enough to cause dust sublimation, the corresponding part of the trajectory is plotted in red. This part of the motion is just a

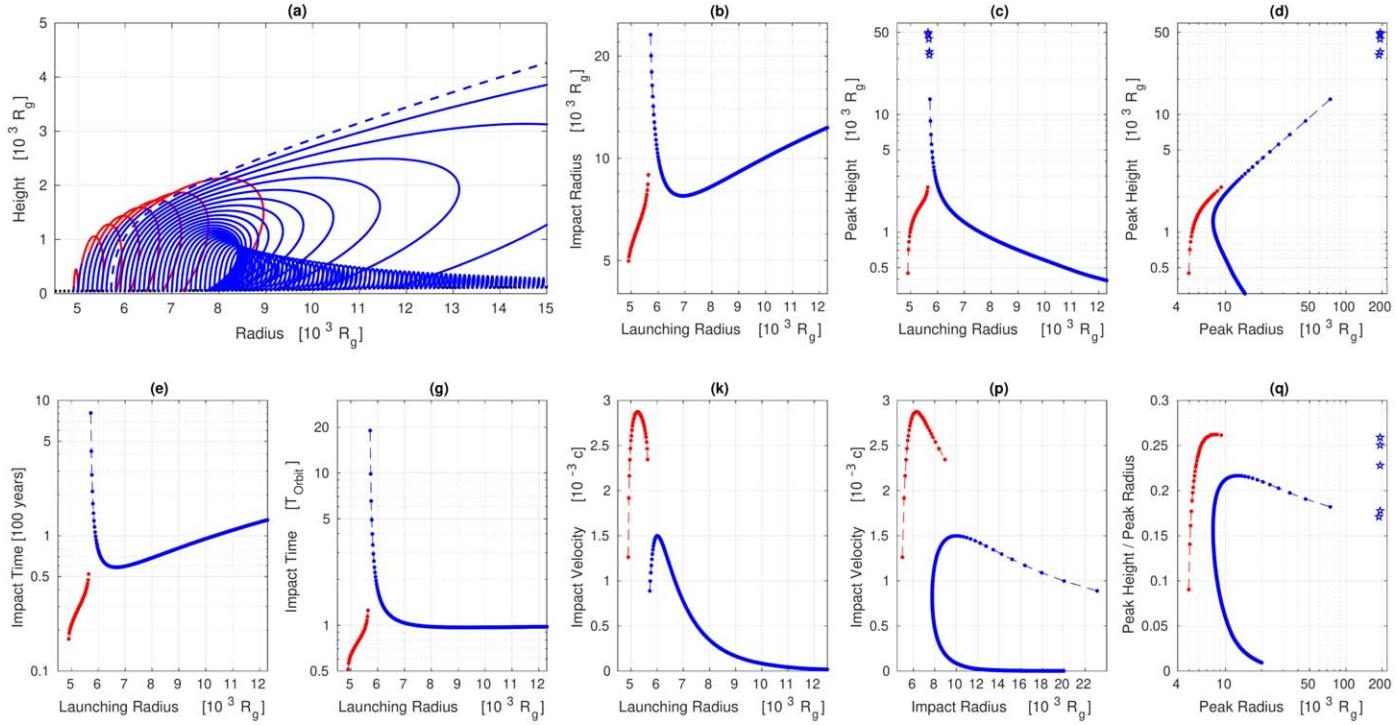

Figure 5. Global parameters of the cloud motion for $\dot{m} = 1$ in the α-patch model with $\alpha = 3$. Escaping clouds are represented by asterisks. (a) The full trajectories of model clouds. Those trajectories in the inner radii starting in blue and followed by red represent those clouds that reach the sublimation location, where they lose their dust content, and subsequently follow a ballistic motion. The trajectories fully in blue are the clouds that remain dusty throughout their time-of-flight. The blue dashed line represents the trajectory of a dusty escaping cloud. (b) The radii at which a launched cloud from a certain radius impacts the disk surface. As can be seen, there is a narrow range of launching radii from which the launched clouds can travel radially very long distances to finally impact the disk surface or even escape. (c) The maximum height a launched cloud from a certain radius can attain. For the same narrow radial range as in the previous subplot, clouds can reach to very high heights or even escape. (d) This can be considered as the shape of the BLR if all clouds are at their highest vertical position. The Peak Radius means the radius at which the cloud is at the maximum height. (e) The time-of-flight of clouds in units of a hundred years, which shows the timescale for the lifetime of BLR clouds. (g) The time-of-flight of BLR clouds in units of local Keplerian orbital time ($T_{\rm Orbit}$). (k) The velocity at which the clouds impact the disk surface. It shows that the clouds launched from inner radii can severely disturb the disk when they hit it. (p) The impact velocity of clouds in terms of where they hit the disk surface. Obviously, the whole radial range from which a cloud can be effectively launched is hit by the falling-back clouds with impact velocities ranging almost from 300 km s^{-1} to 1000 km s^{-1}. (q) The aspect ratio (Peak Height/Peak Radius) as a proxy for the opening angle of the location of the BLR clouds in terms of a point of view from outside. The larger the aspect ratio and the smaller the Peak Radius, the easier the clouds are to be detected from outside. Note that in all subplots from (b) to (q), the actual situation of clouds are color-coded by blue and red for dusty and dustless, respectively.

ballistic motion in the gravitational field of the central BH, without a radiation pressure force. In the dustless falling clouds, the dust cannot form again during ballistic motion until it hits the disk surface, due to the short timescale and low pressure (Elvis et al. 2002). Clouds also perform an orbital motion, and they preserve the original angular momentum they had at the launching radius. We show different perspectives of their trajectories, where the z-axis is perpendicular to the disk plane and the axes x and y are in the plane. We see already from this plot that the character of the motion strongly depends on the Eddington ratio.

3.2.1. Characteristics of Motion at the High Eddington Rate

To show the character of the cloud motion in more representative way, we plot the global parameters of the cloud motion for $\dot{m} = 1$ (high Eddington ratio), as displayed in Figure 5. As before, we code with the red color the clouds that end their evolution without dust. Those subplots show whether the clump is dusty or dustless at the time it hits the disk surface or reaches the peak height. The red color does not mean a cloud was dustless at the time of launching. The majority of clouds complete the motion in less than the local Keplerian timescale and return to the disk, although at a different radius than the launching radius.

As can be seen from Figure 5(a), clouds launched in the outer part of the disk (more than $7 \times 10^3 R_g$) do not rise very high above the disk, and they fall back at the radius not much larger than their starting position. The maximum height is a strong decreasing function of the initial radius in the outer disk. The impact velocity in this region is below 300 (km s^{-1}), but nevertheless it is not negligible. The impact of the failed wind clouds creates additional mechanical heating at the disk surface, which was postulated by many authors unable to model the LIL part of the BLR by just radiative heating (e.g., Joly 1987; Baldwin et al. 2004; Panda et al. 2018, 2020a).

Clouds launched at intermediate radii (roughly within $6–7 \times 10^3 R_g$) complete very extended trajectories; they achieve a considerable height and large radii, but finally they return to much smaller radii again after performing a quasi-elliptic motion because their motion is limited by the conservation of angular momentum set at the launching radius. The impact velocity of these clouds lies within 300 –450 km s^{-1}.

Clouds launched from the inner region (roughly within $5–6 \times 10^3 R_g$) are soon exposed to irradiation strong enough to cause dust sublimation. Although their ballistic motion still brings them to relatively large heights, the radial extension of those orbits is not as large as those of the orbits of the clouds

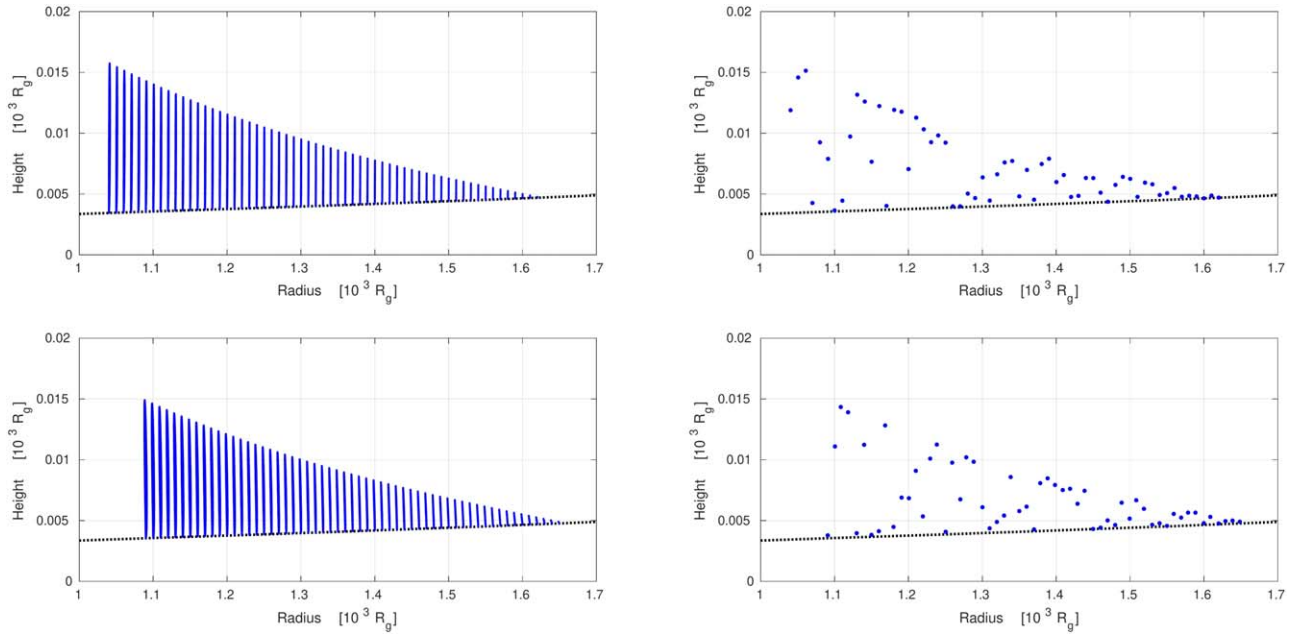

Figure 6. The trajectories of BLR clouds (left panels) and the shape of the BLR in the form of a time snapshot (right panels) calculated from the FRADO model for $\dot{m} = 0.01$. Upper panels: α-patch model of $\alpha = 3$. Lower panels: β-patch model of $\beta = 3$. The black dotted line represents the disk surface.

launched at intermediate radii. The impact velocity of these clouds is the highest, of order 1000 km s^{-1}.

The most interesting orbits are those of clouds launched within a narrow range between the innermost region and the quasi-elliptic motion region, the so-called *escaping zone*. For more details, see Section 3.2.3.

3.2.2. Comparison to Low Eddington Rates

We see from Figure 5 that the character of the motion for the high Eddington ratio depends critically on the launching radius, unlike for the low Eddington ratios, which qualitatively show a simple up and down motion (see Figures 6 and 7). Due to the simplicity of the motion for low Eddington ratios, the results are provided in this paper only for the shielding parameters of α (or β) equal to 3. The Figure 4 shows that sublimation happens mostly at the high Eddington ratio. This also can be seen in Figures 6–9.

As can be seen from Figures 4, 6, and 7, in the case of the low Eddington ratios, the departure of the clouds from the disk surface and the radial extensions of their orbits are not considerable. However, from Figures 4 and 5, for the high Eddington ratio, the height reached and radial range covered by an individual cloud are a significant fraction of the launching radius, and the motion is far more complex. Unlike the cases of low Eddington ratios that show a very simple motion, the case of the high Eddington ratio shows two interesting features due to the complex pattern of motion. They are the formation of a stream of escaping material and also the enhancement of the accretion process at the disk surface due to the complex profile of the landing/launching radius, as described in the following.

The apparently simple motion of the outer dusty clouds at the high Eddington ratio, or all dusty clouds at low Eddington rates, in general have an interesting aspect. Although these clouds do not show a considerable radial motion, their impact onto the disk surface happens at a relatively high angle with respect to the disk (see the third column of Figure 4). This is related to the fact that the vertical velocity before the impact is slowed down by the radiation pressure (see the second column of the same plot), the angular momentum of the cloud is conserved, and the clouds complete almost one local Keplerian orbit, so the cloud takes a trajectory that brings it close to the starting radius. Thus, the impact of the clouds in all cases (not only for innermost clouds in the high Eddington solution) happens at some grazing angle. This could contribute considerably to the development of turbulence in the disk outer layers. It is not clear if such details are resolved in numerical HD simulations because the scale height of this part of the trajectory is quite small.

3.2.3. Stream of Escaping Clouds

The clouds launched within the *escaping zone* escape the radial domain of the computations, set as $\mathrm{BLR_{out}}$, or the inner radius of the dusty torus by definition. More precisely, they do not return to the disk and directly go to torus. This stream of escaping material is relatively narrow, for the model with $\alpha = 3$ the width of the *escaping zone* is $\Delta R = 51\, R_g$, and the zone starts at the distance of $R_{\mathrm{stream}} = 5650\, R_g$. It shows a surprising similarity to the stream postulated purely empirically based on direct observational arguments by Elvis (2000; hereafter EL00). This is also similar to the fast escaping streams in non-HD models (Risaliti & Elvis 2010; Nomura et al. 2013) and HD ones (Proga et al. 1998, 1999, 2000; Proga & Kallman 2004; Sim et al. 2010; Nomura et al. 2020).

Our ratio of the stream width to the distance is indeed very small, ∼0.01 for the adopted parameters, but if the funnel-like structure is densely filled with the BLR clouds, and the cloud's gas number density is $\sim 10^{12}$ cm^{-3}, as argued in the BL18 model and a number of studies (e.g., Adhikari et al. 2016; Panda et al. 2018; Adhikari 2019), the total column density $N_{\mathrm{H}} = n_{\mathrm{H}} \times \Delta R$ across the stream measured close to the disk surface could be as high as 7.5×10^{26} cm^{-2}. Of course, this is only the firm upper limit, as the stream content depends on the details of the outflow launching (see Section 4 for more discussion). Importantly, however, it seems this can be

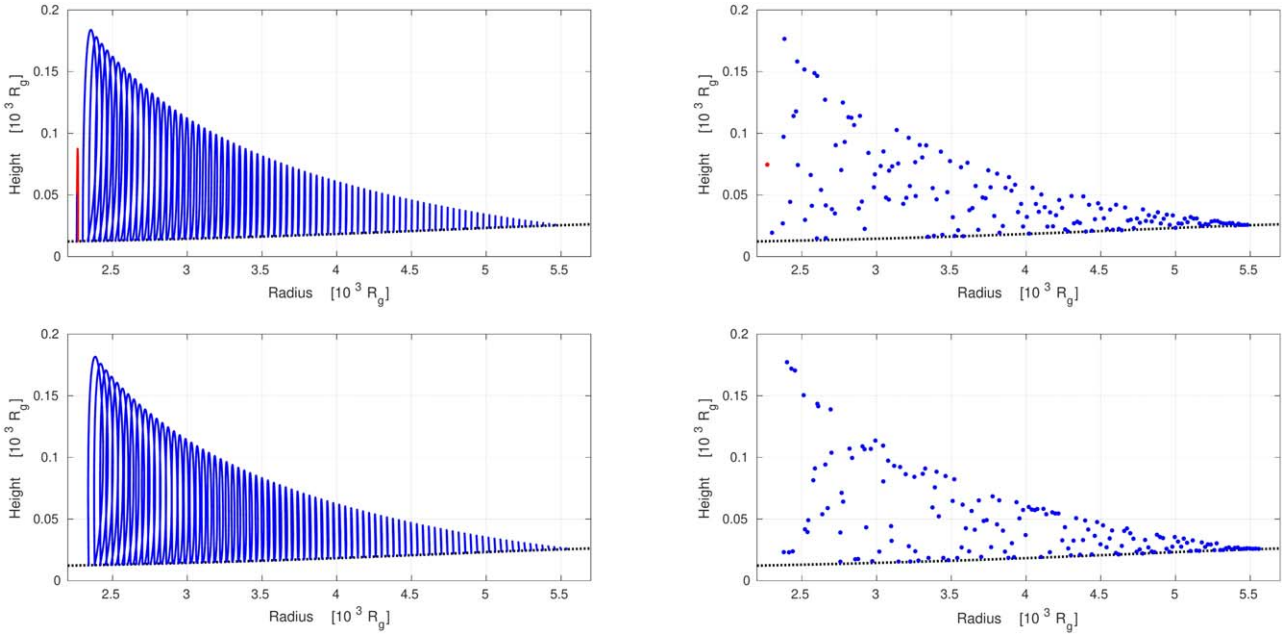

Figure 7. The trajectories of BLR clouds (left panels) and the shape of the BLR in the form of a time snapshot (right panels) calculated from the FRADO model for $\dot{m} = 0.1$. Upper panels: α-patch model of $\alpha = 3$. Lower panels: β-patch model of $\beta = 3$. The black dotted line represents the disk surface.

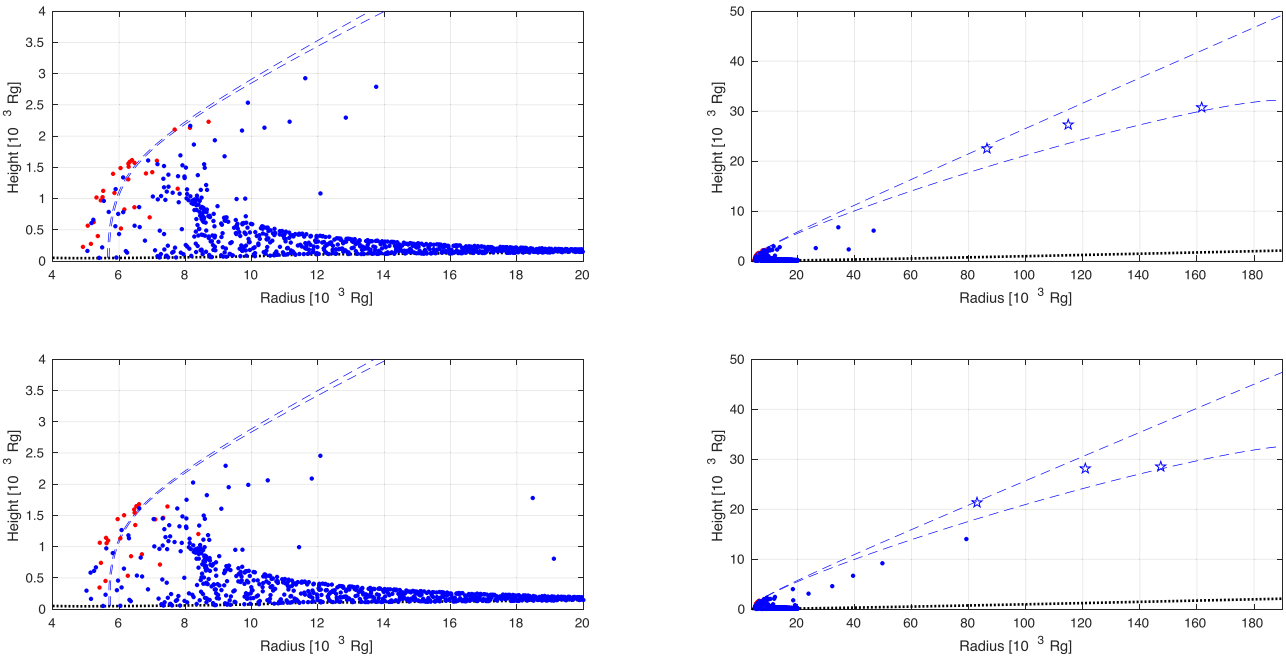

Figure 8. The shape of the BLR calculated from the FRADO model for $\dot{m} = 1$ in the form of a time snapshot. Upper panels: α-patch model of $\alpha = 3$. Lower panels: β-patch model of $\beta = 3$. Right panels are the zoom-out version of the left panels in order to show the extension of the stream up to the torus. The black dotted line represents the disk surface. Escaping clouds are represented by asterisks, and the area covered by escaping clouds is confined within the two blue dashed lines.

evidence that, in the failed wind scenario, the local radiation pressure of the AD can support dusty clumps with very large column densities (Netzer 2015). The asymptotic shape of the stream can be roughly described as a straight line in a 2D perspective in Figures 8 and 9. The inclination angle predicted by the model are around $\sim 74°$ and $\sim 79°$ for α (or β) equal 3 and 5, respectively. These are not much higher than that in EL00 with $\sim 60°$. The line-driven wind models also frequently predict wind that is more focused toward the disk plane (e.g., Higginbottom et al. 2014). The lower part of the stream of material may not ultimately escape, as it shows a decrease in vertical velocity at the outer radius of the computational grid, i.e., BLR_{out}, where we stop the computations. But the upper part of the stream totally escapes because the vertical velocity of material close to BLR_{out} remains constant and its vertical position monotonically increases. This happens due to the fact that we define the torus to be a wall in the outer disk. So if the clouds with highly radially extended trajectories hit the wall (or, equivalently, cross BLR_{out}), they are considered to be the escaping stream. In other words, the

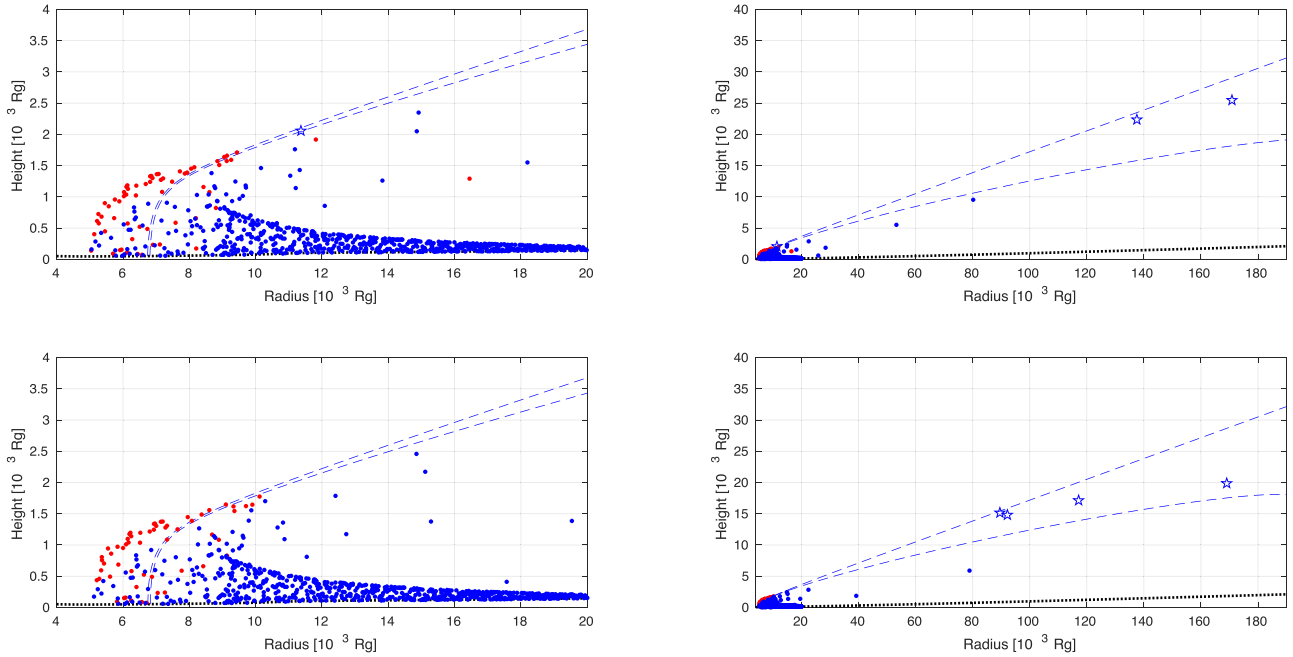

Figure 9. The shape of the BLR calculated from the FRADO model for $\dot{m} = 1$ in the form of a time snapshot. Upper panels: α-patch model of $\alpha = 5$. Lower panels: β-patch model of $\beta = 5$. Right panels are the zoom-out version of the left panels in order to show the extension of the stream up to the torus. The black dotted line represents the disk surface. Escaping clouds are represented by asterisks, and the area covered by escaping clouds is confined within the two blue dashed lines.

condition is based on the location of torus, not on the escape velocity of clouds. As can be seen from Figures 8 and 9, the inclination angle of the stream slightly increases with α (or β).

3.2.4. Landing versus Launching Radius

We notice that, due to part of the radiation pressure coming from the innermost region, the clouds are systematically pushed outwards. This effect is particularly strong in the case of the high accretion rate.

We show the ratio of the landing to starting radius for an exemplary model in Figure 5(b). This systematic return of the clouds to the disk, but at a larger radius, has considerable consequences. First, the cloud motion is calculated assuming a conservation of angular momentum, so the cloud returning to the disk has lower angular momentum than the Keplerian angular momentum at the landing point. This newly arrived lower angular momentum material does not immediately accrete because it gets mixed up with the disk material at the impact, but the net angular momentum at the disk surface (the clumps do not likely enter deeply into the disk) is lower than Keplerian, so the accretion at the disk surface can get enhanced.

3.3. The Shape of the BLR

In parametric models, the BLR is usually represented as a cone filled with the clumps, and the radial and azimuthal cloud densities are assumed to follow a power law and exponential law, respectively (Netzer & Laor 1993; Ward et al. 2014; Adhikari et al. 2016, 2018; Gravity Collaboration et al. 2018).

In our model the shape is determined by the kinematics, and in particular by the maximum height achieved by any cloud for a given initial radius. This shape does not resemble a cone; it rises up relatively fast just after the onset of the BLR, and then the height becomes shallower. The net effect strongly depends on the accretion rate as well as the free parameters of the shielding models.

In order to show the distribution of BLR clouds, we have taken a time snapshot. For this purpose, a flat random number generator is used to choose a random position of a cloud during its flight. Each dot in the Figures 6–9 correspond to a moving cloud in the BLR.

When the accretion rate is low, the height of the BLR is not high, so the clouds remain close to the disk surface, the Keplerian motion remains dominant, and the role of the vertical velocity is small (see Figures 6, 7). We see that for low accretion rates the BLR is close to the disk surface, and in practise such a model cannot be easily distinguished from the irradiated disk surface. Such a model is practically equivalent to the BL18 model. In the present paper we do not yet perform the computations of the shapes of emission lines, but the simple consequence of a small vertical height and small vertical velocity is the expected disk-like line profile. It is interesting to note that this trend is consistent with observational data: low accretion rate sources show frequently double-peak emission lines.

However, when the accretion rate is high, the vertical motion of the clouds is important. The aspect ratio (i.e., the ratio of the local BLR height to that radius) shown in Figure 5(q) reaches 0.27 for dustless clouds and 0.22 for dusty clouds. This maximum aspect ratio is not at the outer radius, but relatively close to the inner radius. We see from Figures 8 and 9 that the overall shape, particularly for the high accretion rate, is very complex. It does not resemble the simple shapes adopted in many numerical BLR models like disks, rings, or shells (Pancoast et al. 2011), or even more complicated but still regular patterns (e.g., Pancoast et al. 2014). It clearly does not support the previously mentioned conical geometry. Instead, for the high accretion rate, a shallowing tail can be seen in Figures 8 and 9 in the shape of the BLR at the outer disk where the Keplerian motion is dominant. This again resembles the results of BL18.

Overall, the calculated BLR shape in our model is similar to that of BL18. However, the FRADO model can also predict the part of the BLR shape missing in BL18 due to the loss of a static solution. Moreover, for the high accretion rate, the model also predicts the stream of escaping material proposed by EL00.

4. Discussion

In this work aimed at developing a dynamical model based on the dust-driven outflow, we followed a non-HD semi-analytical approach to the physics of the BLR. Compared to that in HD models, the description of the dynamics is simplified through approximations described in Section 4.1. Our motivation for this non-HD method is that it allows us to perform a reasonably fast test of the model for a wide range of initial parameters. This advantageous flexibility of our model versus HD models helps later to provide a large dense table grid that can be used for data fitting. Combining the results with a line formation prescription in the next paper, we will be able to compare it to the observational data (mean time delays, line shapes, and transfer functions) for the low ionization part of the BLR.

Our model, though simplified for the purpose of this test, relies on the relatively accurate description of dust-driven dynamics, and later, when combined with outflow rates and line production efficiency, can provide us with a better insight into the BLR and distribution of material than purely parametric models with the density distribution of BLR clouds predetermined as an arbitrary function of the radius and distance from the equatorial plane (e.g., Pancoast et al. 2014; Gravity Collaboration et al. 2020), although some of these models are quite complex (e.g., Matthews et al. 2020), involving a conical outflow and a simple description of clumpiness. Such purely parametric models do not easily test the driving mechanisms. Our model does not have all of the properties of the fully hydrodynamical studies; however, those studies are computationally very expensive. Moreover, before being implemented in an HD context, any model should be tested in an analytical/semi-analytical form. In the following subsections, we will discuss different aspects of the model, compare our results with other BLR studies including HD ones, and address the supporting observational facts.

In this work we calculated the 3D structure of the BLR model within the frame of the FRADO model scenario. This dynamical model of the BLR is based on careful computations of the radiation pressure force acting on clouds launched from the disk surface. We included only the radiation pressure acting on dust and so far have neglected line driving; but, aimed at modeling the LIL part of BLR, this approach may be a good approximation. However, we included the radiation force coming from the extended disk (not the frequently used assumption of a point-like source), and we included a description of the shielding necessary to launch the wind.

Our predicted shape of the BLR depends most significantly on the Eddington ratio. For the high Eddington rate, the launched clouds are accelerated to high velocities at small launch radii, and some of them form a stream of material that is outflowing. At larger radii, a simple failed wind is formed. This outflowing stream shows a striking similarity to the geometrical model of EL00, which is based on observational constraints. At low Eddington ratios, only a failed wind forms in the entire radial range, and vertical velocities and clouds maximum heights are smaller. Despite the presence of turbulence due to the clouds' impact velocity (which is approximately a monotonically decreasing function of radius starting around 110 $\mathrm{km\,s^{-1}}$ (9 $\mathrm{km\,s^{-1}}$) for $\dot{m} = 0.1$ ($\dot{m} = 0.01$) in the inner BLR down to less than 1 $\mathrm{km\,s^{-1}}$ for the last possible trajectory corresponding to the last lifting radius), the BLR resembles somehow a static disk surface. Therefore it shows a considerable similarity to the static BL18 model, in which clouds perform only an orbital motion, while here clouds also have vertical velocities.

The 3D dynamical model is time consuming, so currently some processes are described in a simplified way. This can be improved later on, and here also we do not yet perform a detailed comparison to observational constraints.

4.1. Approximations in the 3D Model

According to the column density of a BLR single cloud (Bianchi et al. 2012), which is of order 10^{23} $\mathrm{cm^{-2}}$, the clouds are moderately optically thick. This is also an assumption of our model, since we use a single-scattering approximation (see the Appendix). If the clouds are optically thick, radiative transfer calculations should be incorporated into our computations, which is beyond the scope of this work. Notably, despite considering the single-scattering approximation, the model produces a powerful and fast outflow, contradicting the results by Costa et al. (2018), who argue an extreme or unrealistic luminosity is required to launch an outflow if single scattering is assumed. It is due to the fact that Costa et al. (2018) consider only the infrared part of the AD spectrum, while in the 3D FRADO model, a broad range of frequencies from the X-ray to UV to infrared contribute to the radiation pressure acting on dust, depending on the actual position of the dusty cloud.

Moreover, the clouds in our model are considered to be very compact, i.e., almost point-like (see the Appendix), while they are loose, extended objects (Bianchi et al. 2012). We do not address the possible collisions between clouds, however, later in Section 4.8 we show it can be a reasonable assumption. The friction with the ambient medium and the instability of clouds due to HD processes are also neglected. However, we discuss our method of treatment of clouds and interactions with the intercloud medium in Section 4.4.

Moreover, our description of the opacity is simpler than the one used in the BL18 model. We assume a fixed single dust sublimation temperature, independent from the grain size and chemical composition. In reality, as in the BL18 model, this temperature depends on the grain size, so the dust evaporation should proceed more slowly as the cloud moves, with smaller grains disappearing first and large grains still providing some radiation force support to the cloud against gravity. This is not yet incorporated in our model.

4.2. Shielding Parameters

We adopted arbitrary values for the two free parameters of α and β in our shielding models. That was due to the fact that we only wanted to test and perceive an overall view of the dynamics of the BLR material and its geometry in the 3D FRADO model with a rough shielding effect included. Obviously, from Figures 6–9, the shape of the BLR depends on the value of the α (or β) parameter, although this dependence is very weak for low Eddington ratios. But the adoptions of the two presented shielding models, either the

α-patch or β-patch, are not clearly distinguishable in terms of the resultant BLR shape. Taking a close look at these figures, it can be seen that, by adopting the β-patch model, the overall shape of the BLR shifts a bit outwards compared to that for the α-patch model. This implies that the wider azimuthal angle in the β-patch model contributes to the total radiative force significantly, while the presence of the outer radii of the disk in the β-patch model is not significant in terms of radiation pressure. So the contribution from large radii can be neglected in the β-patch model as it is in the α-patch model. Thus the α-patch and β-patch models are slightly different only due to the different ranges of azimuthal angles they cover. The α model, however, has an advantage over the β model because it clearly shows that the locally limited radiation pressure of the AD alone is able to lift the material. The α model is consistent with the fact that the field of view of a cloud above the AD is limited due to presence of the ambient medium. The β model takes into account the density gradient in the ambient medium and may be an attractive alternative to the α model when a detailed quantitative comparison with some observational data is done. The results of these models presented in this paper can help us to approach a realistic prescription for the shielding effect in a more physically motivated way, which we aim at in the next papers.

4.3. Static versus Dynamical BLR Model

We stressed in the previous sections that our dynamical model for low Eddington ratios gives qualitatively similar results to BL18. However, some similarities with BL18 exist also for the high Eddington ratio, so only the basic approaches of BL18 and FRADO are different. For the high Eddington ratio, apart from the similar shallowing tail at the outer BLR, BL18 also notice a loss of hydrostatic equilibrium at small radii, and they expect the formation of a wind where their static model does not fully work. The difference is that we follow the dynamical character of the BLR under radiation pressure, while BL18 only report the inability to obtain the static solution. Qualitatively, the loss of the static solution in BL18 happens at a similar location to the location of the *escaping zone* in our model, at about 0.03 pc (see Figure 9 of BL18 and Figures 5, 8, and 9 in this paper). A quantitative comparison is not possible since BL18 use in their Figure 9 a super-solar metallicity ($Z/Z_{\odot} = 5$), while we perform computations assuming a dust-to-gas ratio roughly corresponding to solar metallicity. The important comparison could be done in the future, when line profiles are calculated, and then the difference between the static model and the dynamic model would be likely quite clear.

4.4. Cloud Formation and Stability

The dynamical picture of the clumpy BLR model requires a physical justification of the assumed clumpiness of the medium. This is, however, a complex issue. Wind outflow from the disk is formally launched as a continuous medium, although in the case of a failed wind some level of clumpiness may appear already close to the disk surface. Stellar winds (escaping winds) develop clumpiness at some distance from the star (e.g., Muijres et al. 2011), most likely due to the development of a thermal instability in the irradiated medium. Expectations of the clumpiness were broadly discussed in various contexts (see, e.g., McCourt et al. 2018; Gronke & Oh 2020, and the references therein), and hydrodynamical simulations of this effect are difficult. In the context of AGNs, spontaneous cloud formation from the wind in numerical simulations was reported by Proga & Waters (2015), Waters & Proga (2016, 2019), and Waters et al. (2021), but the cold clumps falling down were found only in the last paper, which studies much larger radii of accretion flow (well within the dusty torus), but still excludes the dust content. So, the situation in the context of the BLR clouds at the expected distances is not clear.

As for the stability, the simple evaluation of the destruction (due to ablation or evaporation) of the clouds, taking into account the electron conduction and irradiation (A. L. Müller et al. 2021, in preparation), gives timescales of order 100 yr, which is comparable to the orbital timescales. That said, some very short episodes of X-ray absorption have been identified in individual BLR clouds (Risaliti et al. 2011; Torricelli-Ciamponi et al. 2014), most likely those exceptionally high above the disk surface so they were still along the line of sight toward the observer. The observational constraints for the clouds from eclipse (Pietrini et al. 2019) imply cloud sizes of 10^{13} cm for a $10^{8} M_{\odot}$ BH mass. Other reports of the AGN clumpy medium such as that by Markowitz et al. (2014) contain a mixture of shorter events caused by the BLR clouds and longer events related to the dusty/molecular torus clouds, which prevents one from drawing a firm observational conclusion. Most of the clouds located very close to the disk are never seen in absorption since their presence (potentially visible in highly inclined sources) is hidden from the observer by a dusty torus.

Clouds are also unstable due to the Kelvin–Helmholtz (KH) process, for which a characteristic timescale can be estimated (see, e.g., Peißker et al. 2020). The timescale for the growth of KH instabilities (for clouds of the size as in our model) is of order a few days (A. L. Müller et al. 2021, in preparation). This is much shorter than the flight time of clouds, implying the likely complete destruction of clouds before landing; however, magnetized clouds can cope with KH instabilities (McCourt et al. 2015) and survive longer (Shin et al. 2008). In addition, there are also a number of HD simulations that show an efficient acceleration of dusty material and a longer survival time despite the destructive role of such instabilities (see, e.g., Davis et al. 2014; Tsang & Milosavljević 2015; Zhang & Davis 2017; Zhang et al. 2018).

4.5. The Effects of Cloud−disk Collisions

Failed wind clouds returning to the disk bring several additional aspects that are not deeply discussed in the current paper. We briefly discussed in Section 3.2.4 the landing issue in our model, in terms of angular momentum. The impact radius of the cloud is always larger than the formation radius, which is due to the larger radiation flux from smaller disk radii. Since clouds preserve angular momentum, in this way we have a systematic departure from the strictly Keplerian angular momentum at the disk surface due to the cloud impact. This may enhance the surface layer accretion, since the effective angular momentum there becomes sub-Keplerian.

The next effect is due to the mechanical impact, which is considerable in the case of clouds on elongated orbits, so called *nonlocal clouds*, present in the $\dot{m} = 1$ solution and less important for clouds with landing radii close to the starting radius. We can estimate the depth at which the cloud material is

deposited inside the disk by a simple comparison of the ram pressure with the gas pressure inside the disk, knowing the disk vertical structure including the density, temperature, and pressure profile. For models discussed in this paper and an Eddington ratio of 0.01, the clouds are stopped at a height of order 10–20% lower than the total disk height, while for *nonlocal clouds* and an Eddington ratio of 1.0 clouds graze at up to ∼50% of the total disk height. The impact leads to shock formation and nonthermal emission from particles accelerated in these shocks (A. L. Müller et al. 2021, in preparation).

The impact will lead to the destruction of the dust in the inner part of the BLR region, where the surface temperature of the unperturbed disk is below the dust sublimation temperature, but clouds penetrating the disk reach layers where the temperature is higher. High velocity clouds impacting occasionally at larger radii can do that as well. The dust there is destroyed by the mechanical heating at the impact. However, the medium at the impact is rather dense, with the local number density $n_{\rm impact}$ of the plasma above 10^{15} cm^{-3}, so it cools efficiently. If we use the cooling function $\Lambda(T)$ provided by Gnat & Ferland (2012), we can see that the kinetic energy of impact, of order $n_{cl}\, m_p\, v_{\rm impact}^2$ per unit mass, can be re-emitted in a timescale of order seconds

$$t_{\rm cool} = \frac{n_{cl}\, m_p\, v_{\rm impact}^2}{\Lambda(T)\, n_{\rm impact}^2} \sim 1 \ ({\rm s}) \qquad (15)$$

assuming the gas temperature T is of order 10^4 K and assuming that the cooling medium is still optically thin, as is the whole cloud. The key issue is then the origin of the dust. If the dust must arrive from larger radii (e.g., from the outer dusty/molecular torus), then of course the accretion process would be very long. However, as was argued by Elvis et al. (2002) and used in the proposed FRADO model of Czerny & Hryniewicz (2011), the conditions in the outer layers of the disk are perfect for the dust formation in situ. Efficient dust formation requires well-defined pressure and temperature conditions, and high densities in the disk allow for these conditions to be satisfied. The conditions of dust formation are best studied in the case of stars; the details of the early stage of the dust formation are still unclear (the issue of dust seeds—see, e.g., Ventura et al. 2012), but dust formation actually happens in the stellar wind, at distances of up to a few stellar radii, so the timescales must correspond to the wind outflow timescales, set by the wind velocity, of order a few tens of km s^{-1} (e.g., Goldman et al. 2017), which is of order days up to a year. Such a timescale is much shorter than the time separation between the two cloud impacts at a given location, since the cloud impact events are separated by the timescale of order fraction of the local orbital (Keplerian) timescale, which is about 100 yr. Therefore, the dust destruction is only temporary, and the dust content in the disk atmosphere is recovered between impacts.

4.6. The Fast Outflow Stream

High velocities of escaping material, which can extend to very large distances triggered by disk radiation pressure, have been addressed in a number of papers (Hopkins & Elvis 2010; Harrison et al. 2014; Ishibashi & Fabian 2015; Thompson et al. 2015; Ishibashi et al. 2017; Costa et al. 2020).

The stream-like feature of the outflow predicted empirically by El00 was previously shown in HD simulations by Proga et al. (1998, 1999, 2000). More studies later also showed the development of such a feature in an HD context (see, e.g., Proga & Kallman 2004; Sim et al. 2010; Nomura et al. 2020) and even in non-HD models (Risaliti & Elvis 2010; Nomura et al. 2013).

While the models mentioned above focus on line-force on the BLR gas, which most likely corresponds to the HIL of the BLR, this work is the first study to hint at the development of such a feature also at larger distances, in the LIL BLR (not the torus), as a result of radiation pressure acting on dust. The stream is highly inclined and focused more toward the AD with an inclination of ∼70–80°, consistent with observations (Gravity Collaboration et al. 2018) and sophisticated HD models (e.g., Proga et al. 2000; Proga & Kallman 2004; Nomura et al. 2020). However, it initiates at larger radii of few $10^3 R_g$ responsible for the LIL BLR, compared to a few $10^2 R_g$ in HD studies (also see Sim et al. 2010; Higginbottom et al. 2014) where the HIL BLR develops. The feature in our model is seen only for the case of the high Eddington rate, but an enhancement of the metallicity and the dust-to-gas ratio to more typical super-solar values in AGNs can give rise to the same feature even in lower accretion rate sources. Thus, we would expect two separate streams of material, at two different distances from the BHs.

4.7. FRADO Predictions versus Observations

As discussed above, our reasonably justified model is also fast enough compared to HD models to produce results for a large grid of initial physical parameters. We believe that the negligence of hydro effects is not very important. As argued by Risaliti & Elvis (2010), the motion in the radiative acceleration phase and later the motion of the clump in the medium are highly supersonic, so the effect of the pressure gradient to change the density and the internal pressure of the clouds can be neglected. The fact that our simple description recovers the motion complexity seems to support this view. Thus, an approximate description may be good enough for testing if indeed the radiation pressure acting on dust drives the motion of the BLR clouds.

4.7.1. RL Relation

The FRADO model well predicts the basic location of the LIL BLR (Czerny & Hryniewicz 2011; Czerny et al. 2017), and the estimates using shielding allowed us to recover the radius −luminosity (RL) relation, including the dispersion (Naddaf et al. 2020). The earlier studies indicated a rather tight relation, but new reverberation mapping results indicate considerable dispersion in the RL relation (Czerny et al. 2019; Du & Wang 2019; Fonseca Alvarez et al. 2020; Martínez-Aldama et al. 2020). This dispersion, which is apparently different depending on the broad line that is adopted as the indicator (Zhang et al. 2021), is most likely related to a spread in the Eddington ratio (e.g., Du et al. 2016; Naddaf et al. 2020; Zajaček et al. 2020, 2021), which reflects the spread in the optical/UV spectral energy distribution and the available ionizing flux (Fonseca Alvarez et al. 2020).

A preliminary test of our results with observations can be done as follows. For the high Eddington rate, we consider the radius most densely impacted with falling clouds, covering a

broad range of aspect ratios, i.e., $8000R_g$, as shown in Figures 5(p) and (q), to be the location of the BLR. As for the low Eddington rates, the location of the BLR is taken to be where the highest peak is attained by clouds, most likely to be visible to the observer, which is around $2400R_g$ and $1100R_g$ as shown in Figures 6 and 7 for rates of 0.1 and 0.01, respectively. We calculate the time delays for the viewing angle of $i = 39.2°$ (Lawrence & Elvis 2010) and for both the clouds located in the [closer—farther] side of the AD relative to the observer using

$$\tau = \frac{R_{\rm BLR}}{c}(\sqrt{1+q^2} \pm \sin i - q\cos i) \quad (16)$$

where q is the aspect ratio, as in Figure 5(q). The value of q is negligible for low Eddington rates, while for the high rate we take the median value of $q = 0.15$. It gives [4.57–20.42], [10–44.67], and [23.44–138] days for the Eddington rates of 0.01, 0.1, and 1, respectively. We can compare these limits with the transfer function for the Hβ line determined observationally. For example, the transfer function in Mrk 817, with a BH mass of $(4.9 \pm 0.8) \times 10^7$ (Peterson & Horne 2004) and an Eddington ratio of 0.14 (Li et al. 2016), mostly peaks in the range of 10–30 days (Li et al. 2016), which seems to be consistent with our predictions given above for these accretion parameters. It must be stressed here again that in our model the location of the BLR depends only on the assumption of the dust sublimation temperature, and gives the location of the LIL part of the BLR. A detailed study of the RL relation and the transfer function measurements based on the model will be addressed in the next paper.

4.7.2. Line Shapes and Ratios

In the current paper we do not address the issue of the line shapes and ratios, since this requires a complex approach, such as those in typical parametric models (e.g., Pancoast et al. 2014). Our model predicts the radiation flux seen by the clouds, but indeed the cloud density will have to be parameterized. We can start from the assumption of a constant cloud density, since its quite universal value is supported by the line ratio fitting in the LIL BLR (e.g., Adhikari et al. 2016; Panda et al. 2018; Adhikari 2019). Later we can limit the freedom by assuming the power-law radial distribution of the density of the hot intercloud medium, and then determine the cloud density as a function of the radius from the pressure balance or pressure confinement (Różańska et al. 2006; Baskin & Laor 2018). We expect that our more complex dynamics will give single-peak Lorentzian profiles not only for extremely low viewing angles (e.g., Goad et al. 2012), but also for moderate inclinations in the case of high Eddington ratio objects.

4.7.3. BLR and Torus

It has been matter of debate, due to many studies based on interferometry (e.g., Clavel et al. 1989; Swain et al. 2003; Kishimoto et al. 2009, 2011; Pott et al. 2010; Gravity Collaboration et al. 2020) and RM (e.g., Suganuma et al. 2006; Koshida et al. 2014; Schnülle et al. 2015; Minezaki et al. 2019), whether dust is located within the BLR radii or it only sets the outer radius of the BLR, defining the *dusty torus*. Our new sophisticated 3D FRADO model predicts the launch of dusty material from the disk due to AD radiation pressure as the mechanism of formation of the BLR whose trajectories can extend to large radii and high altitudes that can be responsible for the formation of torus. The results of complex flying material above the disk surface are consistent with the findings of studies by Goad et al. (2012) and Figaredo et al. (2020). It also shows that the emission of the BLR and dusty region are interrelated, as confirmed by Wang et al. (2013).

The dusty torus has been introduced for masking the central disk from observation at high inclinations due to presence of a large amount of dust of high column densities extending from the equatorial plane to high altitudes (Antonucci & Miller 1985). The structure is not likely to be static, but a possible scenario involves the interaction between the outflows and inflows to form a geometrically thick torus (Wada 2012). Lawrence & Elvis (2010) suggested distorted/misaligned disks as the obscurer.

In most scenarios proposed so far for the formation of dusty torus, a sublimation radius is defined based on the condition of surviving dust from the spherical AD radiation field. The radius sets the onset of the dusty torus, the first radius from which dust survives the intense radiation of the whole AD at any altitude above the disk. However, the question is what brings the dusty material to those high altitudes. Therefore, a dynamical model of the wind was proposed for the torus itself (e.g., Konigl & Kartje 1994; Elitzur & Shlosman 2006; Gallagher et al. 2015), but this was not a failed wind. The dust location is constrained in an interesting observational study by Markowitz et al. (2014) covering mostly high Eddington rate sources. It gives a radial domain spanning $0.3–140 \times 10^4\, R_g$ for the location of BLR clouds. This implies that clouds are partially in the outer dusty torus, but partially in the BLR. However, the outflow of BLR clouds toward the torus, as in our results for the high Eddington rate, and in other studies (e.g., Kawaguchi & Mori 2010, 2011; Goad et al. 2012; Hönig 2019; Figaredo et al. 2020), can provide some momentum to the claim that the dusty torus is a posterior to the BLR and is indeed part of it; however, this view is far from being widely and firmly accepted.

4.7.4. The Mass Outflow Rate

In order to estimate the ejected mass from the AD due to radiation pressure within the *escaping zone*, we assume that the clouds are optically thin at the time of launching. So the optical depth of the cloud, τ, in the vertical direction can be of order one. The Planck mean at sublimation radius is almost 50 times the Thompson value (see Figure 1). One can obtain the column density of $N_{\rm H}^{\rm vert} = 3 \times 10^{22}\,{\rm cm}^{-2}$ in the vertical direction, according to $\tau = N_{\rm H}^{\rm vert} \times \sigma_{\rm Pl}$ where $\sigma_{\rm Pl}$ is the Planck mean opacity. It is much higher than the column density in the horizontal direction, as discussed in Section 3.2. We are thus able to approximate the total flow of the vertically ejected mass as

$$\dot{M}_{\rm outflow} = \frac{2\pi\, R_{\rm l}\, \Delta R\, N_{\rm H}}{t_{\rm exit}} = 1.1152 \times 10^{23}\,{\rm g\,s^{-1}} \quad (17)$$

where $R_{\rm l} = 5680\ R_g$ is a launching radius within the *escaping zone*, $\Delta R = 51\ R_g$ is the width of the *escaping zone*, and $t_{\rm exit} = 1.79 \times 10^8$ s is the time it takes for the ejected material at $R_{\rm l}$ to leave the *escaping zone*. Compared to the whole accretion rate of $\dot{M}_{\rm edd} = 1.399 \times 10^{26}\,{\rm g\,s^{-1}}$ for accretion rate of $\dot{m} = 1$ and the adopted $M_{\rm BH} = 10^8 M_\odot$, the value is small. Although it does not perturb the whole accretion process, it is not negligible, either. However, this implies the modeled stream

of material does not explain the BAL QSO flow (Borguet et al. 2013) where the outflow is massive. So the huge amount of material must come from somewhere else, most probably from some circumnuclear rings, etc.

4.8. Number of Clouds and Probable Collisions

Taking an upper limit for the mass-loss rate of the entire disk at the high Eddington rate, i.e., 10^{24} g s^{-1}, one can simply estimate the total number of BLR clouds at any given moment, and also the mean flight time between two successive direct collisions of clouds. The mass of BLR clouds of typical size 10^{12}–10^{13} cm and typical density 10^{12} up to 10^{13} cm^{-3} lies in the range of 10^{24}–10^{28} g, which corresponds to the launching of 10^{-4} up to 1 cloud per second. Combining with the flight time of clouds of around several tens of years (as implied by Figure 5), we obtain a total number of 10^{5}–10^{9} clouds building the BLR.

A simple formula from thermodynamics yields the collision timescale of clouds as

$$\tau_{\rm coll} = \frac{\lambda}{\bar{v}} = \frac{1}{\sqrt{2}\, n_{\rm cl}\, \sigma\, \bar{v}} \tag{18}$$

where $\bar{v}$ is the average velocity of clouds, which in this case is of order 1000 km s^{-1}, and λ is the *mean free path* where $n_{\rm cl}$ is the volume number density of clouds, and σ is their collision cross section. It can be rewritten as

$$\tau_{\rm coll} \simeq 0.1\, \frac{R_{\rm BLR}^3\, n_{\rm H}\, m_{\rm p}\, R_{\rm cloud}}{\dot{M}_{\rm outflow}\, t_{\rm flight}\, \bar{v}} \tag{19}$$

for a very geometrically flattened, shallow BLR, with a height of order 0.1 times its radial size. Recasting it for a BLR of typical radial size 10^{17} cm, we have

$$\tau_{\rm coll} \simeq 20 \left(\frac{n_{\rm H}}{10^{12}\ {\rm cm}^{-3}}\right)\left(\frac{R_{\rm cloud}}{10^{12}\ {\rm cm}}\right)\left(\frac{100\ {\rm yr}}{t_{\rm flight}}\right){\rm yr}. \tag{20}$$

This is almost the minimum value for the collision timescale, since the flight times of clouds are mostly less than 100 yr (see Figure 5(e)), and also a minimum value for $n_{\rm H}$ or $R_{\rm cloud}$ and an upper limit for the disk mass-loss rate are adopted. It therefore implies that direct encounters are not highly probable, such that the clouds may experience one collision during a full orbit. So neglect of the adjustment of a given cloud trajectory due to adjacent trajectories is a relatively safe assumption in our calculation.

4.9. Dusty BLR Studies in an HD Context

Our description of the dynamics relying on the presence of dust and the important role of dust driving in the BLR, although simplified, shows good potential to address observational features, as discussed in Section 4.7. However, the results for the dynamics from our model cannot be compared yet with HD simulations, since these simulations did not aim to address the dusty BLR. Instead, there is a long list of HD studies and/or advanced physically based studies aimed to model the dusty torus (e.g., Konigl & Kartje 1994; Dorodnitsyn et al. 2012; Wada 2012; Chan & Krolik 2016, 2017; Hönig 2019; Williamson et al. 2019; Huang et al. 2020) or assuming the line-driven mechanism (e.g., Murray et al. 1995; Proga et al. 2000; Higginbottom et al. 2014; Waters et al. 2016, 2021; Waters & Proga 2016). Torus-modeling papers assume the inner radius of their structure at the location with dust sublimation temperature calculated from the total bolometric flux, so the temperature of the medium is lower than in the BLR. We know from observations that this region is a factor of ∼5 larger than the BLR radius measured from the Hβ line delay (Koshida et al. 2014). Papers based on line-driven winds predict a BLR radius that is too small for LIL such as Hβ. For example, in Proga et al. (2000), the outflowing stream starts at 7 light days (for a BH mass of $10^8\ M_\odot$ and an Eddington ratio of 0.5), which is rather more appropriate for HIL lines (also see Waters & Proga 2016), while our dust-based model gives 27 days, as expected for Hβ. We therefore have to look forward to future HD models that incorporate dust-related mechanisms in BLR dynamics.

The future development of realistic HD models for the dusty BLR will be certainly difficult, as hinted at by rather advanced dust/gas dynamics modeling done in the context of proto-planetary disks (see, e.g., Vinković & Čemeljić 2021). Another important issue in HD simulations is that the clumps in current simulations, either dusty or gaseous, are of very low density, very large size, and/or very far from the center (e.g., Waters et al. 2021) compared to dense small BLR clouds of size 10^{12} up to 10^{13} cm (e.g., Risaliti et al. 2011; Pietrini et al. 2019) located closer to the central irradiating source. Regarding the typical size of a BLR of order 10^{17} cm, one needs to have a spatial resolution of $\sim 10^{-4}$ or better in order to resolve a single BLR cloud, which has not yet been reached by highly time- and computational-expensive 2D or 3D HD simulations. Alternatively, we can just rely on the observational facts to test the model, and this is the path we plan to take in the near future.

5. Summary

We tested the dynamics of the BLR under the 2.5D non-HD prescription of the FRADO model. In this test we incorporated into the model wavelength-dependent dust opacities and two proposed configurations for the shielding effect.

As the results imply, the model is similar to the BL18 model of a static puffed-up disk, although the FRADO model catches the whole dynamical shape of the BLR, most importantly for the high accretion rate, where BL18 noticed the loss of the static solution. The FRADO model also predicts the thin-funnel-like stream of escaping material proposed in the EL00 model for the high accretion rate.

The shape of the BLR for the high accretion rate seems to be very complicated and does not show any resemblance to the usually adopted shapes for the BLR including disks, rings, shells, or cones. It is intuitively expected to produce single-peak emission profiles for the high accretion rate. However, we expect to have disk-like line profiles (double-peak emission lines) for low accretion rates due to simple up/down motions of clouds with small vertical heights and velocities. We will calculate the shape of line profiles and examine their dependence on accretion rates and other parameters in the next paper.

The model shows that it may account for the LIL part of the BLR. We previously performed a preliminary test of the model with the radius−luminosity (RL) relation. It was successful in explaining the observed dispersion in the Hβ RL relation based on the Eddington ratio. In our next paper, we will consider time-delay measurements resulting from the 3D FRADO model in full detail.

The project was partially supported by the Polish Funding Agency National Science Centre, project 2017/26/A/ST9/00756 (MAESTRO 9), and MNiSW grant DIR/WK/2018/12. The authors would like to thank D. Semenov for helpful information he provided us on dust opacities. The authors are also grateful to the referee for the fruitful comments that considerably improved the quality of the paper.

Appendix
Physical Calculations

A.1. Radiation Pressure from an Extended Luminous Disk Acting on a Single Cloud

The computations of the dusty cloud motion are based on the determination of the radiation pressure from the extended accretion disk. Our approach is basically similar to the computations done by Icke (1980), but the medium opacity there was described by a wavelength-independent Thomson cross section for electron scattering, which reduces the problem considerably. Here, we use a complex description of the opacity, and the computation of the force from a given disk part depends not only on the relative geometrical position of the disk/cloud system, but also on the disk local temperature. Computations of the radiative force from the line-driven wind in a number of papers (e.g., Pereyra et al. 1997; Proga et al. 1998; Feldmeier & Shlosman 1999) were also done by integrating the force over the extended disk, but in these papers no integration is performed over the wavelength for a specific contribution from the disk, and only the local disk flux is important, not the spectral shape. Moreover, the line-driven force indeed depends on the velocity gradient, which complicates considerably the dynamical computations. In the case of dust radiation pressure, no coupling with velocity is present, but the wavelength integration, grain size distribution, and chemical composition are important, as it allows automatically for the inclusion of the UV and infrared force component. We also take care of the effects of scattering and absorption separately. Since this integration over wavelength is an important aspect of the computations, we present the details of the method below.

The time-independent radiation pressure due to absorption and scattering by definition (Mihalas 1978) are

$$P^{\rm abs} = \frac{1}{c}\int\int I_\lambda(\boldsymbol{r}, \hat{\boldsymbol{s}})\,\cos\alpha\; d\Omega\; d\lambda \tag{A1}$$

$$P^{\rm sca} = \frac{2}{c}\int\int I_\lambda(\boldsymbol{r}, \hat{\boldsymbol{s}})\,\cos^2\alpha\; d\Omega\; d\lambda \tag{A2}$$

where I is the intensity of the radiating object, c the speed of light, and α is the angle between the unit vector $\hat{\boldsymbol{s}}$ and the normal to the area element $\hat{\boldsymbol{n}}_A$ shown in Figure 10(a). Therefore the absorption- and scattering-driven radiative acceleration of an infinitesimal object (dA) irradiated by an infinitesimal emitter (dB) shown in Figure 10(a) are

$$\boldsymbol{a}^{\rm abs} = \frac{1}{Mc}\int\int I_\lambda\;\sigma_\lambda^{\rm abs}\;\cos\alpha\;\hat{\boldsymbol{s}}\;d\Omega\;d\lambda \tag{A3}$$

$$\boldsymbol{a}^{\rm sca} = \frac{2}{Mc}(-\hat{\boldsymbol{n}}_A)\int\int I_\lambda\;\sigma_\lambda^{\rm sca}\;\cos^2\alpha\;d\Omega\;d\lambda \tag{A4}$$

where M is the mass of irradiated object (the receiver), and σ_ν is the cross section of the irradiated object for absorption or scattering, which in general is frequency dependent. It should be noted that we have used σ_ν rather than dA, which is applicable provided that the gradient of radiation pressure across the irradiated object (receiver) is negligible. It implies a small receiver (or, equivalently, grains with small values of cross sections).

Assuming the effective cross section of the receiver to be always perpendicular to $\hat{\boldsymbol{s}}$, so $\alpha = 0$, and we have

$$\boldsymbol{a}^{\rm abs}_{\rm grain} = \frac{1}{M_{\rm grain}}\frac{1}{c}\int\int I_\lambda\;\sigma_\lambda^{\rm abs}\;\hat{\boldsymbol{s}}\;d\Omega\;d\lambda \tag{A5}$$

$$\boldsymbol{a}^{\rm sca}_{\rm grain} = \frac{1}{M_{\rm grain}}\frac{2}{c}\int\int I_\lambda\;\sigma_\lambda^{\rm sca}\;\hat{\boldsymbol{s}}\;d\Omega\;d\lambda \tag{A6}$$

so the total radiative acceleration of the object is

$$\boldsymbol{a}^{\rm rad}_{\rm grain} = \frac{1}{M_{\rm grain}}\frac{1}{c}\int\int I_\lambda\;\sigma_\lambda^{\rm rad}\;\hat{\boldsymbol{s}}\;d\Omega\;d\lambda \tag{A7}$$

where $\sigma_\lambda^{\rm rad} = \sigma_\lambda^{\rm abs} + 2\sigma_\lambda^{\rm sca}$.

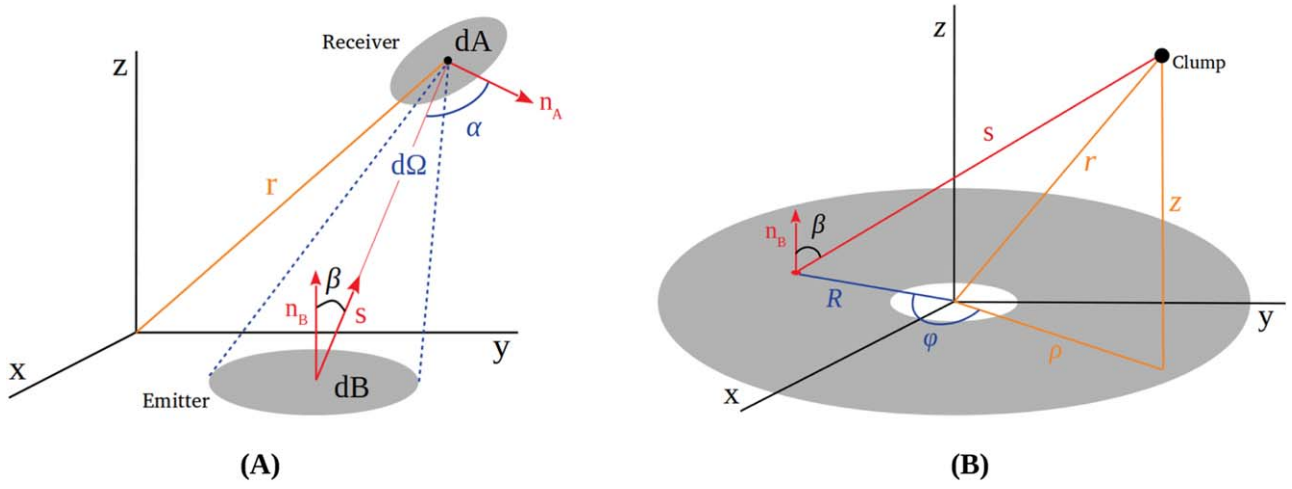

Figure 10. (a) Geometry of the emitter−receiver system, which resembles the disk−cloud system for a differential (infinitesimal) segment of the disk. (b) Geometry of the disk−cloud system.

Using the definition of solid angle, we consider an extended disk-like radiating surface shown in Figure 10(a) in gray, where the red spot is the area element in polar coordinates, dB, shown in the Figure 10(b), and $\hat{\boldsymbol{n}}_B$ is the unit vector normal to dB. So we have

$$d\Omega = \frac{\cos\beta}{s^2}\, R\, dR\, d\varphi \tag{A8}$$

where $\cos\beta = z/s$, and $\hat{\boldsymbol{s}} = \boldsymbol{s}/s$. So we have

$$\boldsymbol{a}^{\rm rad}_{\rm grain} = \frac{1}{M_{\rm grain}}\frac{z}{c}\int\int\int I_\lambda\, \sigma^{\rm rad}_\lambda\, \frac{\mathbf{s}}{s^4}\, R\, dR\, d\varphi\, d\lambda. \tag{A9}$$

Knowing that $\boldsymbol{s} = \boldsymbol{r} - \boldsymbol{R}$, using the below definitions

$$\begin{cases} \boldsymbol{r} = & \rho & \hat{\rho} + & z & \hat{\boldsymbol{z}} \\ \boldsymbol{R} = & R\cos\varphi & \hat{\rho} + & R\sin\varphi & \hat{\rho}_\perp \end{cases} \tag{A10}$$

we can obtain the vector $\boldsymbol{s}$ and its length as

$$\boldsymbol{s} = (\rho - R\cos\varphi)\,\hat{\rho} - R\sin\varphi\,\hat{\rho}_\perp + z\,\hat{\boldsymbol{z}} \tag{A11}$$

$$s^2 = r^2 + R^2 - 2\,\rho\,R\cos\varphi. \tag{A12}$$

Due to azimuthal symmetry, the summation over the second term of $\boldsymbol{s}$ would give zero, so we have

$$\boldsymbol{a}^{\rm rad}_{\rm grain} = \frac{1}{M_{\rm grain}}\frac{z}{c}\int\int\int I_\lambda\, \sigma^{\rm rad}_\lambda \times \frac{(\rho - R\cos\varphi)\,\hat{\rho} + z\,\hat{\boldsymbol{z}}}{(r^2 + R^2 - 2\rho R\cos\varphi)^2}\, R\, dR\, d\varphi\, d\lambda \tag{A13}$$

for which one can have the components in Cartesian coordinates just using $\hat{\rho} = (x\,\hat{x} + y\,\hat{y})/\rho$.

This is different from the approach of Icke (1980) in terms of the denominator. In the definition of $\hat{\boldsymbol{s}} = \boldsymbol{s}/s$, we can remove the second term of $\hat{\boldsymbol{s}}$ due to azimuthal symmetry, but it can not be removed from s (the magnitude of $\hat{\boldsymbol{s}}$). However, this mistake did not propagate in the literature.

This gives the net radiative acceleration for a single grain of a specific size and certain type of material. But for a dusty clump, i.e., a distribution of dust particles (with different materials and different sizes) embedded in and strongly coupled with a volume of gas, the radiative acceleration can be obtained by summation over the type and size of dust particles as below

$$\boldsymbol{a}^{\rm rad}_{\rm clump} = \frac{1}{M_{\rm clump}}\frac{z}{c}\int\int\int I_\lambda\, \sigma^{\rm tot(rad)}_\lambda \times\frac{(\rho - R\cos\varphi)\,\hat{\rho} + z\,\hat{\boldsymbol{z}}}{(r^2 + R^2 - 2\rho R\cos\varphi)^2}\, R\, dR\, d\varphi\, d\lambda \tag{A14}$$

where $M_{\rm clump} = M_{\rm dust} + M_{\rm gas}$.

The final form of radiative acceleration for the dusty clump is

$$\boldsymbol{a}^{\rm rad}_{\rm clump} = \frac{\Psi}{1+\Psi}\frac{z}{c}\int_{\lambda_i}^{\lambda_f}\int_{\varphi_{\min}}^{\varphi_{\max}} \times\int_{R_{\min}}^{R_{\max}} I_\lambda\, K^{\rm rad}_\lambda\, \frac{(\rho - R\cos\varphi)\,\hat{\rho} + z\,\hat{\boldsymbol{z}}}{(r^2 + R^2 - 2\,\rho\,R\cos\varphi)^2}\, R\, dR\, d\varphi\, d\lambda \tag{A15}$$

where Ψ is the clump dust-to-gas ratio, and $K^{\rm rad}_\lambda$ is the mean total cross section per dust mass, which resembles the definition of opacity (see Appendix A.2 for details).

Incorporating the radiation pressure on w-percent ionized gas, one can generally write

$$\boldsymbol{a}^{\rm rad}_{\rm clump} = \frac{1}{M_{\rm clump}}\frac{F}{c}(\sigma^{\rm tot}_{\rm dust} + \sigma^{\rm tot}_{\rm T}) \tag{A16}$$

which can be rewritten as

$$\boldsymbol{a}^{\rm rad}_{\rm clump} = \frac{\mathbb{F}}{c}\left(\frac{\Psi}{1+\Psi}\,K^{\rm rad}_{\rm dust} + \frac{w}{1+\Psi}\,\frac{\sigma^{\rm tot}_{\rm T}}{M_{\rm ion.gas}}\right) \approx \frac{\mathbb{F}}{c}\left(\Psi\,K^{\rm rad}_{\rm dust} + w\,\frac{\sigma_{\rm T}}{m_{\rm p}}\right) \tag{A17}$$

so if the first term dominates the second term, the radiation pressure due to Thompson electron scattering can be neglected (see Figure 1).

It should be noted that we have considered the strong-coupling approximation. So the clump is a unified rigid body within which the embedded spherical dust particles and the volume of gas are spatially fixed as if wired or connected to each other. Also the clump is not of a large size, or the dust particles are mostly concentrated around its center. Otherwise, randomly oriented acceleration vectors of dust particles located at random positions within a large volume of gas will result in a different net acceleration vector. This becomes worse if there is no dust−gas strong coupling, which results in deformation, disintegration, and fragmentation of the clump.

A.2. Dust Opacity and Dust-to-gas Ratio

In order to find $\sigma^{\rm tot(rad)}_\lambda$, assuming a dust model with a population of dust types with a given grain size distribution, we proceed with a general relation valid for grains with radius $a_- \leqslant a \leqslant a_+$ as below

$$dn_i(a) = n\, f_i(a)\, da = n_i(a)\, da \tag{A18}$$

where $n_i(a)$ is the number density of grains and n is the number density of H nuclei ($n = n_{\rm H} + 2n_{H_2}$), i stands for the dust type, and f_i is a modular function. Now one can write, for example, the total absorption cross section (the same applies to the total scattering cross section) for a given dust type as

$$\sigma^{\rm tot(abs)}_{\lambda,i} = V_{\rm clump}\int_{a_-^i}^{a_+^i} n_i(a)\,[\sigma(a)]^{\rm abs}_{\lambda,i}\, da \tag{A19}$$

where $[\sigma(a)]^{\rm abs}_{\lambda,i}$ is the absorption cross section of a single grain of a certain sort of size a (radius) at wavelength λ, and $V_{\rm clump}$ is the volume of the clump. Summation over types of dust gives

$$\sigma^{\rm tot(abs)}_\lambda = \textstyle\sum_{i=1}^{\rm NDS}\sigma^{\rm tot(abs)}_{\lambda,i} = V_{\rm clump}\textstyle\sum_{i=1}^{\rm NDS}\displaystyle\int_{a_-^i}^{a_+^i} n_i(a)\,[\sigma(a)]^{\rm abs}_{\lambda,i}\, da \tag{A20}$$

where NDS is the number of dust types in the dust model. Likewise we can find $\sigma^{\rm tot(sca)}_\lambda$ and consequently $\sigma^{\rm tot(rad)}_\lambda$.

When calculating the radiative acceleration, it would be easier to work with general densities, ratios, and mean values rather than certain masses or volumes. Looking at Equation (A14) we can write

$$\frac{\sigma^{\rm tot(rad)}_\lambda}{M_{\rm clump}} = \frac{M_{\rm dust}}{M_{\rm clump}}\frac{\sigma^{\rm tot(rad)}_\lambda}{M_{\rm dust}} = \frac{\Psi}{1+\Psi}\,K^{\rm rad}_\lambda \tag{A21}$$

where $K_\lambda^{\rm rad}$ is the total opacity of the clump given by

$$K_\lambda^{\rm rad} = K_\lambda^{\rm abs} + 2K_\lambda^{\rm sca} \tag{A22}$$

where

$$K_\lambda^{j} = \frac{1}{\Psi}\sum_{i=1}^{\rm NDS} K_{\lambda,i}^{j}\Psi_i \tag{A23}$$

where

$$K_{\lambda,i}^{j} = \frac{\sigma_{\lambda,i}^{{\rm tot}(j)}}{M_{{\rm dust},i}} = \frac{1}{\rho_{{\rm dust},i}}\int_{a_-^i}^{a_+^i} n_i(a)\,[\sigma(a)]_{\lambda,i}^{j}\,da \tag{A24}$$

where j stands for (rad), (abs), or (sca); and Ψ is dust-to-gas mass ratio given by

$$\Psi = \frac{M_{\rm dust}}{M_{\rm gas}} = \frac{\rho_{\rm dust}}{\rho_{\rm gas}} = \sum_{i=1}^{\rm NDS}\Psi_i = \frac{\sum_{i=1}^{\rm NDS}\int_{a_-^i}^{a_+^i} n_i(a)\,4/3\pi a^3\rho_{{\rm b},i}\,da}{nm_{\rm H}} = \frac{\sum_{i=1}^{\rm NDS}\int_{a_-^i}^{a_+^i} f_i(a)\,4/3\pi a^3\rho_{{\rm b},i}\,da}{m_{\rm H}} \tag{A25}$$

where $\rho_{{\rm b},i}$ is the bulk dust density of type i, and $m_{\rm H}$ is the mass of H nuclei.

A.3. Dust Sublimation

Assuming instantaneous re-emission of the absorbed radiation by dust in the form of isotropic blackbody radiation, if the amount of heat absorbed by the dusty content of the clump increases its temperature to that of sublimation, the radiative engine of motion of the clump switches off. So the criterion for the sublimation of dusty content is

$$E_{\rm abs} = E_{\rm emit}(T_{\rm s}). \tag{A26}$$

The total radiative energy by definition (Mihalas 1978) is

$$E = \int I_\lambda(\boldsymbol{r}, \hat{\boldsymbol{n}})\,\cos(\alpha)\,d\lambda\,dA\,d\Omega\,dt. \tag{A27}$$

So the radiative energy absorbed by dust is

$$E_{\rm abs} = \int I_\lambda\,\sigma_\lambda^{\rm tot(abs)}\,d\lambda\,d\Omega\,dt \tag{A28}$$

and the energy re-emitted by dust (Loska et al. 1993) at the sublimation temperature ($T_{\rm s}$) is

$$E_{\rm emit}(T_{\rm s}) = 4\pi\int B_\lambda(T_{\rm s})\,\sigma_\lambda^{\rm tot(abs)}\,d\lambda\,dt. \tag{A29}$$

Dividing both sides of Equation (A26) by dt and $M_{\rm dust}$ we can introduce Q (the total power per dust mass), so we have $Q_{\rm abs} = Q_{\rm emit}(T_{\rm s})$ for the sublimation criterion where

$$Q_{\rm emit}(T_{\rm s}) = 4\pi\int B_\lambda(T_{\rm s})\,K_\lambda^{\rm abs}\,d\lambda \tag{A30}$$

$$Q_{\rm abs} = \int I_\lambda\,K_\lambda^{\rm abs}\,d\lambda\,d\Omega \tag{A31}$$

so we have

$$Q_{\rm abs} = z\int_{\lambda_i}^{\lambda_f}\int_{\varphi_{\rm min}}^{\varphi_{\rm max}}\int_{R_{\rm min}}^{R_{\rm max}}\frac{I_\lambda\,K_\lambda^{\rm abs}}{(r^2+R^2-2\rho R\cos\varphi)^{3/2}}\times R\,dR\,d\varphi\,d\lambda. \tag{A32}$$

ORCID iDs

Mohammad-Hassan Naddaf https://orcid.org/0000-0002-7604-9594
Bożena Czerny https://orcid.org/0000-0001-5848-4333
Ryszard Szczerba https://orcid.org/0000-0003-2886-4460

References

Adhikari, T. P. 2019, Photoionization Modelling as a Density Diagnostic of Line Emitting/Absorbing Regions in Active Galactic Nuclei (Cham: Springer International Publishing)
Adhikari, T. P., Hryniewicz, K., Różańska, A., Czerny, B., & Ferland, G. J. 2018, ApJ, 856, 78
Adhikari, T. P., Różańska, A., Czerny, B., Hryniewicz, K., & Ferland, G. J. 2016, ApJ, 831, 68
Antonucci, R. R. J., & Miller, J. S. 1985, ApJ, 297, 621
Balbus, S. A., & Hawley, J. F. 1991, ApJ, 376, 214
Baldwin, J. A., Ferland, G. J., Korista, K. T., Hamann, F., & LaCluyzé, A. 2004, ApJ, 615, 610
Barvainis, R. 1987, ApJ, 320, 537
Baskin, A., & Laor, A. 2018, MNRAS, 474, 1970
Begelman, M. C., McKee, C. F., & Shields, G. A. 1983, ApJ, 271, 70
Bianchi, S., Maiolino, R., & Risaliti, G. 2012, AdAst, 2012, 782030
Blandford, R. D., & Begelman, M. C. 1999, MNRAS, 303, L1
Blandford, R. D., & McKee, C. F. 1982, ApJ, 255, 419
Blandford, R. D., & Payne, D. G. 1982, MNRAS, 199, 883
Borguet, B. C. J., Arav, N., Edmonds, D., Chamberlain, C., & Benn, C. 2013, ApJ, 762, 49
Boroson, T. A., & Green, R. F. 1992, ApJS, 80, 109
Brotherton, M. S., Wills, B. J., Steidel, C. C., & Sargent, W. L. W. 1994, ApJ, 423, 131
Capriotti, E., Foltz, C., & Byard, P. 1980, ApJ, 241, 903
Chan, C.-H., & Krolik, J. H. 2016, ApJ, 825, 67
Chan, C.-H., & Krolik, J. H. 2017, ApJ, 843, 58
Chau Giang, N., & Hoang, T. 2020, arXiv:2009.06958
Clavel, J., Wamsteker, W., & Glass, I. S. 1989, ApJ, 337, 236
Collin, S., & Zahn, J.-P. 1999, A&A, 344, 433
Collin, S., & Zahn, J. P. 2008, A&A, 477, 419
Collin-Souffrin, S., Dyson, J. E., McDowell, J. C., & Perry, J. J. 1988, MNRAS, 232, 539
Costa, T., Pakmor, R., & Springel, V. 2020, MNRAS, 497, 5229
Costa, T., Rosdahl, J., Sijacki, D., & Haehnelt, M. G. 2018, MNRAS, 473, 4197
Croton, D. J., Springel, V., White, S. D. M., et al. 2006, MNRAS, 365, 11
Czerny, B., Du, P., Wang, J.-M., & Karas, V. 2016, ApJ, 832, 15
Czerny, B., & Hryniewicz, K. 2011, A&A, 525, L8
Czerny, B., Li, J., Loska, Z., & Szczerba, R. 2004a, MNRAS, 348, L54
Czerny, B., Li, Y.-R., Hryniewicz, K., et al. 2017, ApJ, 846, 154
Czerny, B., Modzelewska, J., Petrogalli, F., et al. 2015, AdSpR, 55, 1806
Czerny, B., Olejak, A., Rałowski, M., et al. 2019, ApJ, 880, 46
Czerny, B., Różańska, A., & Kuraszkiewicz, J. 2004b, A&A, 428, 39
Davis, S. W., Jiang, Y.-F., Stone, J. M., & Murray, N. 2014, ApJ, 796, 107
Done, C., & Krolik, J. H. 1996, ApJ, 463, 144
Donea, A.-C., & Protheroe, R. J. 2002, PASA, 19, 39
Dong, X., Wang, T., Wang, J., et al. 2008, MNRAS, 383, 581
Dorodnitsyn, A., Kallman, T., & Bisnovatyi-Kogan, G. S. 2012, ApJ, 747, 8
Du, P., Lu, K.-X., Zhang, Z.-X., et al. 2016, ApJ, 825, 126
Du, P., & Wang, J.-M. 2019, ApJ, 886, 42
Elitzur, M., & Shlosman, I. 2006, ApJL, 648, L101
Elvis, M. 2000, ApJ, 545, 63
Elvis, M., Marengo, M., & Karovska, M. 2002, ApJL, 567, L107
Everett, J. E. 2005, ApJ, 631, 689
Feldmeier, A., & Shlosman, I. 1999, ApJ, 526, 344

Figaredo, C. S., Haas, M., Ramolla, M., et al. 2020, AJ, 159, 259
Fonseca Alvarez, G., Trump, J. R., Homayouni, Y., et al. 2020, ApJ, 899, 73
Fukumura, K., Tombesi, F., Kazanas, D., et al. 2015, ApJ, 805, 17
Gallagher, S. C., & Everett, J. E. 2007, in ASP Conf. Ser. 373, The Central Engine of Active Galactic Nuclei, ed. L. C. Ho & J. W. Wang (San Francisco, CA: ASP), 305
Gallagher, S. C., Everett, J. E., Abado, M. M., & Keating, S. K. 2015, MNRAS, 451, 2991
Gaskell, C. M. 2009, NewAR, 53, 140
Gaskell, C. M., Goosmann, R. W., Antonucci, R. R. J., & Whysong, D. H. 2004, ApJ, 616, 147
Gnat, O., & Ferland, G. J. 2012, ApJS, 199, 20
Goad, M. R., Korista, K. T., & Ruff, A. J. 2012, MNRAS, 426, 3086
Goldman, S. R., van Loon, J. T., Zijlstra, A. A., et al. 2017, MNRAS, 465, 403
Gravity Collaboration, Amorim, A., Bauböck, M., et al. 2021, A&A, 648, A117
Gravity Collaboration, Dexter, J., Shangguan, J., et al. 2020, A&A, 635, A92
Gravity Collaboration, Sturm, E., Dexter, J., et al. 2018, Natur, 563, 657
Grier, C. J., Peterson, B. M., Horne, K., et al. 2013, ApJ, 764, 47
Gronke, M., & Oh, S. P. 2020, MNRAS, 494, L27
Grzedzielski, M., Janiuk, A., Czerny, B., & Wu, Q. 2017, A&A, 603, A110
Hagino, K., Odaka, H., Done, C., et al. 2015, MNRAS, 446, 663
Harrison, C. M., Alexander, D. M., Mullaney, J. R., & Swinbank, A. M. 2014, MNRAS, 441, 3306
Higginbottom, N., Knigge, C., Long, K. S., Sim, S. A., & Matthews, J. H. 2013, MNRAS, 436, 1390
Higginbottom, N., Proga, D., Knigge, C., et al. 2014, ApJ, 789, 19
Hirai, Y., & Fukue, J. 2001, PASJ, 53, 285
Hönig, S. F. 2019, ApJ, 884, 171
Hopkins, P. F., & Elvis, M. 2010, MNRAS, 401, 7
Hopkins, P. F., Strauss, M. A., Hall, P. B., et al. 2004, AJ, 128, 1112
Hosseinirad, M., Abbassi, S., Roshan, M., & Naficy, K. 2018, MNRAS, 475, 2632
Hu, C., Wang, J.-M., Ho, L. C., et al. 2008, ApJ, 687, 78
Huang, X., Davis, S. W., & Zhang, D. 2020, ApJ, 893, 50
Icke, V. 1980, AJ, 85, 329
Ishibashi, W., Banerji, M., & Fabian, A. C. 2017, MNRAS, 469, 1496
Ishibashi, W., & Fabian, A. C. 2015, MNRAS, 451, 93
Joly, M. 1987, A&A, 184, 33
Jun, H. D., Assef, R. J., Carroll, C. M., et al. 2021, ApJ, 906, 21
Kartje, J. F., Königl, A., & Elitzur, M. 1999, ApJ, 513, 180
Kawaguchi, T., & Mori, M. 2010, ApJL, 724, L183
Kawaguchi, T., & Mori, M. 2011, ApJ, 737, 105
Khajenabi, F. 2016, ApJ, 828, 9
Kishimoto, M., Hönig, S. F., Antonucci, R., et al. 2009, A&A, 507, L57
Kishimoto, M., Hönig, S. F., Antonucci, R., et al. 2011, A&A, 527, A121
Konigl, A., & Kartje, J. F. 1994, ApJ, 434, 446
Koshida, S., Minezaki, T., Yoshii, Y., et al. 2014, ApJ, 788, 159
Krause, M., Burkert, A., & Schartmann, M. 2011, MNRAS, 411, 550
Lawrence, A., & Elvis, M. 2010, ApJ, 714, 561
Lawrence, A., Elvis, M., Wilkes, B. J., McHardy, I., & Brandt, N. 1997, MNRAS, 285, 879
Le, H. A. N., & Woo, J.-H. 2019, ApJ, 887, 236
Leftley, J. H., Hönig, S. F., Asmus, D., et al. 2019, ApJ, 886, 55
Li, A. 2007, in ASP Conf. Ser. 373, The Central Engine of Active Galactic Nuclei, ed. L. C. Ho & J. W. Wang (San Francisco, CA: ASP), 561
Li, Y.-R., Wang, J.-M., & Bai, J.-M. 2016, ApJ, 831, 206
Liu, Y., & Zhang, S. N. 2011, ApJL, 728, L44
Loska, Z., Szczerba, R., & Czerny, B. 1993, MNRAS, 261, 63
Marconi, A., Axon, D. J., Maiolino, R., et al. 2008, ApJ, 678, 693
Markowitz, A. G., Krumpe, M., & Nikutta, R. 2014, MNRAS, 439, 1403
Martínez-Aldama, M. L., Zajaček, M., Czerny, B., & Panda, S. 2020, ApJ, 903, 86
Mas-Ribas, L. 2019, ApJ, 885, 95
Mas-Ribas, L., & Mauland, R. 2019, ApJ, 886, 151
Mathis, J. S., Rumpl, W., & Nordsieck, K. H. 1977, ApJ, 217, 425
Matthews, J. H., Knigge, C., Higginbottom, N., et al. 2020, MNRAS, 492, 5540
McCourt, M., Oh, S. P., O'Leary, R., & Madigan, A.-M. 2018, MNRAS, 473, 5407
McCourt, M., O'Leary, R. M., Madigan, A.-M., & Quataert, E. 2015, MNRAS, 449, 2
Mihalas, D. 1978, Stellar Atmospheres (2nd ed.; San Francisco, CA: Freeman)
Minezaki, T., Yoshii, Y., Kobayashi, Y., et al. 2019, ApJ, 886, 150
Miniutti, G., Saxton, R. D., Rodríguez-Pascual, P. M., et al. 2013, MNRAS, 433, 1764
Mioc, V., & Radu, E. 1992, AN, 313, 353
Mizumoto, M., Done, C., Tomaru, R., & Edwards, I. 2019, MNRAS, 489, 1152
Mizumoto, M., Nomura, M., Done, C., Ohsuga, K., & Odaka, H. 2021, MNRAS, 503, 1442
Mosallanezhad, A., Yuan, F., Ostriker, J. P., Zeraatgari, F. Z., & Bu, D.-F. 2019, MNRAS, 490, 2567
Muijres, L. E., de Koter, A., Vink, J. S., et al. 2011, A&A, 526, A32
Murray, N., & Chiang, J. 1995, ApJL, 454, L105
Murray, N., Chiang, J., Grossman, S. A., & Voit, G. M. 1995, ApJ, 451, 498
Naddaf, M.-H., Czerny, B., & Szczerba, R. 2020, FrASS, 7, 15
Netzer, H. 2013, The Physics and Evolution of Active Galactic Nuclei (Cambridge: Cambridge University Press)
Netzer, H. 2015, ARA&A, 53, 365
Netzer, H., & Laor, A. 1993, ApJL, 404, L51
Netzer, H., Lutz, D., Schweitzer, M., et al. 2007, ApJ, 666, 806
Netzer, H., & Marziani, P. 2010, ApJ, 724, 318
Nomura, M., Ohsuga, K., & Done, C. 2020, MNRAS, 494, 3616
Nomura, M., Ohsuga, K., Wada, K., Susa, H., & Misawa, T. 2013, PASJ, 65, 40
Oknyansky, V. L., Gaskell, C. M., & Shimanovskaya, E. V. 2015, OAP, 28, 175
Osterbrock, D. E. 1978, PhyS, 17, 285
Pancoast, A., Brewer, B. J., & Treu, T. 2011, ApJ, 730, 139
Pancoast, A., Brewer, B. J., & Treu, T. 2014, MNRAS, 445, 3055
Panda, S. 2020, A&A, 650, A154
Panda, S., Czerny, B., Adhikari, T. P., et al. 2018, ApJ, 866, 115
Panda, S., Czerny, B., Done, C., & Kubota, A. 2019a, ApJ, 875, 133
Panda, S., Martínez-Aldama, M. L., Marinello, M., et al. 2020a, ApJ, 902, 76
Panda, S., Marziani, P., & Czerny, B. 2019b, ApJ, 882, 79
Panda, S., Marziani, P., & Czerny, B. 2020b, CoSka, 50, 293
Peißker, F., Eckart, A., Sabha, N. B., Zajaček, M., & Bhat, H. 2020, ApJ, 897, 28
Pereyra, N. A., Kallman, T. R., & Blondin, J. M. 1997, ApJ, 477, 368
Peterson, B. M. 1993, PASP, 105, 247
Peterson, B. M., & Horne, K. 2004, AN, 325, 248
Peterson, B. M., Wanders, I., Horne, K., et al. 1998, PASA, 110, 660
Pietrini, P., Torricelli-Ciamponi, G., & Risaliti, G. 2019, A&A, 628, A26
Plewa, P. M., Schartmann, M., & Burkert, A. 2013, MNRAS, 431, L127
Pott, J.-U., Malkan, M. A., Elitzur, M., et al. 2010, ApJ, 715, 736
Proga, D. 2007, ApJ, 661, 693
Proga, D., & Kallman, T. R. 2004, ApJ, 616, 688
Proga, D., Stone, J. M., & Drew, J. E. 1998, MNRAS, 295, 595
Proga, D., Stone, J. M., & Drew, J. E. 1999, MNRAS, 310, 476
Proga, D., Stone, J. M., & Kallman, T. R. 2000, ApJ, 543, 686
Proga, D., & Waters, T. 2015, ApJ, 804, 137
Raimundo, S. I., Vestergaard, M., Goad, M. R., et al. 2020, MNRAS, 493, 1227
Raouf, M., Silk, J., Shabala, S. S., et al. 2019, MNRAS, 486, 1509
Rees, M. J., Silk, J. I., Werner, M. W., & Wickramasinghe, N. C. 1969, Natur, 223, 788
Reeves, J. N., & Turner, M. J. L. 2000, MNRAS, 316, 234
Reissl, S., Klessen, R. S., Mac Low, M.-M., & Pellegrini, E. W. 2018, A&A, 611, A70
Richards, G. T., Hall, P. B., Vanden Berk, D. E., et al. 2003, AJ, 126, 1131
Rieke, G. H. 1978, ApJ, 226, 550
Risaliti, G., & Elvis, M. 2010, A&A, 516, A89
Risaliti, G., Nardini, E., Salvati, M., et al. 2011, MNRAS, 410, 1027
Różańska, A., Czerny, B., Życki, P. T., & Pojmański, G. 1999, MNRAS, 305, 481
Różańska, A., Goosmann, R., Dumont, A. M., & Czerny, B. 2006, A&A, 452, 1
Röllig, M., Szczerba, R., Ossenkopf, V., & Glück, C. 2013, A&A, 549, A85
Saslaw, W. C. 1978, ApJ, 226, 240
Schmidt, M. 1963, Natur, 197, 1040
Schnülle, K., Pott, J. U., Rix, H. W., et al. 2015, A&A, 578, A57
Semenov, D., Henning, T., Helling, C., Ilgner, M., & Sedlmayr, E. 2003, A&A, 410, 611
Seyfert, C. K. 1943, ApJ, 97, 28
Shadmehri, M. 2015, MNRAS, 451, 3671
Shakura, N. I., & Sunyaev, R. A. 1973, A&A, 500, 33
Shangguan, J., Ho, L. C., & Xie, Y. 2018, ApJ, 854, 158
Shapovalova, A. I., Popović, L. Č., Burenkov, A. N., et al. 2010, A&A, 509, A106
Shen, Y., Richards, G. T., Strauss, M. A., et al. 2011, ApJS, 194, 45
Shin, M.-S., Stone, J. M., & Snyder, G. F. 2008, ApJ, 680, 336

Shlosman, I., Vitello, P. A., & Shaviv, G. 1985, ApJ, 294, 96
Sim, S. A., Proga, D., Miller, L., Long, K. S., & Turner, T. J. 2010, MNRAS, 408, 1396
Suganuma, M., Yoshii, Y., Kobayashi, Y., et al. 2006, ApJ, 639, 46
Sulentic, J. W., Marziani, P., & Dultzin-Hacyan, D. 2000, ARA&A, 38, 521
Swain, M., Vasisht, G., Akeson, R., et al. 2003, ApJL, 596, L163
Szczerba, R., Omont, A., Volk, K., Cox, P., & Kwok, S. 1997, A&A, 317, 859
Tazaki, R., Ichikawa, K., & Kokubo, M. 2020, ApJ, 892, 84
Temple, M. J., Banerji, M., Hewett, P. C., Rankine, A. L., & Richards, G. T. 2020, MNRAS, 501, 3061
Thompson, T. A., Fabian, A. C., Quataert, E., & Murray, N. 2015, MNRAS, 449, 147
Torricelli-Ciamponi, G., Pietrini, P., Risaliti, G., & Salvati, M. 2014, MNRAS, 442, 2116
Tsang, B. T. H., & Milosavljević, M. 2015, MNRAS, 453, 1108
Ventura, P., di Criscienzo, M., Schneider, R., et al. 2012, MNRAS, 420, 1442
Vinković, D., & Čemeljić, M. 2021, MNRAS, 500, 506
Voit, G. M. 1992, MNRAS, 258, 841
Wada, K. 2012, ApJ, 758, 66
Wandel, A., Peterson, B. M., & Malkan, M. A. 1999, ApJ, 526, 579
Wang, H., Xing, F., Zhang, K., et al. 2013, ApJL, 776, L15
Wang, J.-M., Cheng, C., & Li, Y.-R. 2012a, ApJ, 748, 147
Wang, J.-M., Du, P., Baldwin, J. A., et al. 2012b, ApJ, 746, 137
Wang, J.-M., Du, P., Brotherton, M. S., et al. 2017, NatAs, 1, 775
Wang, J.-M., Ge, J.-Q., Hu, C., et al. 2011, ApJ, 739, 3
Wang, J.-M., Qiu, J., Du, P., & Ho, L. C. 2014, ApJ, 797, 65
Ward, R. L., Wadsley, J., & Sills, A. 2014, MNRAS, 445, 1575
Watarai, K.-y., & Fukue, J. 1999, PASJ, 51, 725
Waters, T., Kashi, A., Proga, D., et al. 2016, ApJ, 827, 53
Waters, T., & Proga, D. 2016, MNRAS, 460, L79
Waters, T., & Proga, D. 2019, ApJ, 875, 158
Waters, T., Proga, D., & Dannen, R. 2021, ApJ, 914, 62
Weingartner, J. C., & Draine, B. T. 2001, ApJ, 548, 296
Williamson, D., Hönig, S., & Venanzi, M. 2019, ApJ, 876, 137
Witt, H. J., Czerny, B., & Zycki, P. T. 1997, MNRAS, 286, 848
Zafar, T., Møller, P., Watson, D., et al. 2015, A&A, 584, A100
Zajaček, M., Czerny, B., Martinez-Aldama, M. L., et al. 2020, ApJ, 896, 146
Zajaček, M., Czerny, B., Martinez-Aldama, M. L., et al. 2021, ApJ, 912, 10
Zhang, D., & Davis, S. W. 2017, ApJ, 839, 54
Zhang, D., Davis, S. W., Jiang, Y.-F., & Stone, J. M. 2018, ApJ, 854, 110
Zhang, X., He, Z., Wang, T., & Guo, H. 2021, ApJ, 914, 143